INL/EXT-21-62750

M3 milestone: Advanced contact 2021

September 2021

Dewen Yushu, Antonio Recuero, Daniel Schwen, Alexander Lindsay, and Benjamin Spencer

Idaho National Laboratory, Idaho Falls, ID 83415, USA

INL/EXT-21-62750

M3 milestone: Advanced contact 2021

Dewen Yushu, Antonio Recuero, Daniel Schwen, Alexander Lindsay, and Benjamin Spencer

Idaho National Laboratory, Idaho Falls, ID 83415, USA

September 2021

Idaho National Laboratory
Computational Mechanics and Materials Department
Idaho Falls, Idaho 83415

http://www.inl.gov

Prepared for the
U.S. Department of Energy
Office of Nuclear Energy
Under DOE Idaho Operations Office
Contract DE-AC07-05ID14517

Page intentionally left blank

Contents

1 Background **1**
- 1.1 Node-to-segment formulation . . . 1
- 1.2 Mortar formulation . . . 2
- 1.3 Outstanding issues and vision . . . 2

2 Governing equations **3**
- 2.1 Mechanical model . . . 3
- 2.2 Thermal model . . . 5
- 2.3 Finite element discretization . . . 5
- 2.4 Code implementation . . . 7

3 Dual mortar and preconditioner **7**
- 3.1 Dual mortar for contact . . . 7
- 3.2 Variable condensation preconditioner . . . 9
- 3.3 VCP for thermomechanical contact . . . 11

4 Mechanical contact benchmark problems **12**
- 4.1 Hertzian contact (cylinder on a plane) . . . 12
- 4.2 Ironing problem . . . 17

5 Thermomechanical contact with mortar in BISON **20**
- 5.1 Pellet with missing surface . . . 20
- 5.2 LWR fuel rods . . . 23
  - 5.2.1 Smeared pellets . . . 24
  - 5.2.2 Discrete pellets . . . 25
  - 5.2.3 Discrete pellets with friction (mortar) . . . 27
- 5.3 Application of VCP in BISON . . . 29
- 5.4 Novel reactor geometry . . . 30
- 5.5 Migration guide . . . 31

6 Conclusions and future work **32**

References **33**

Page intentionally left blank

Milestone title

Implement advanced contact approaches for use in emerging reactors with geometries that differ from LWR/EBR-II cylindrical fuel. Due 5/20/2021

Milestone description

Contact remains a challenging and crucially important component of our modeling toolkit. While significant improvements have been made through mortar and automatic differentiation, we would like to explore further approaches such as Nitsche's method, which yields better-conditioned systems and will improve the robustness and performance of BISON contact problems. This effort is relevant to emerging reactor types (e.g., microreactors) and their numerous corresponding complex contact surfaces.

1 Background

This section outlines the available formulations for contact modeling in BISON, ongoing work, and longer-term development goals proposed in response to the modeling of emerging reactor designs.

1.1 Node-to-segment formulation

BISON features a number of contact formulations routinely used for well-established models such as light-water reactor (LWR) pellet-clad thermomechanical interaction. In particular, node-to-segment (NTS) formulations compute fluxes and contact pressures by enforcing constraints in a point-wise manner. Within this category, we may distinguish the following options:

1. **Kinematic** A mechanical contact kinematic approach enforces the gap constraint exactly (i.e., at each nonlinear step), and the node locations of the secondary surface that are identified to be in contact are forced to lie on the primary surface.

2. **Tangential penalty** The normal contact component is enforced exactly, whereas the tangential component resulting from Coulomb's law is computed using a penalty coefficient applied to the incremental slip vector in an iterative manner.

3. **Full penalty** The penalty approach used to compute tangential forces can be extended to the normal contact forces to yield a fully penalty-based formulation.

These three variations of NTS formulations enable users to select the formulation that best performs for each particular modeling scenario. For frictional problems, the tangential penalty approach frequently enables better convergence than the full kinematic approach. Numerical convergence of the overall physical system usually becomes a subject of concern when using frictional contact in practical problems. The stick-slip local behavior defined by inequality constraints causes the nonlinear system to lack the necessary smoothness requirements. The following strategies are available to alleviate this effect:

1. **Augmented Lagrange method** This approach adds and outer nested loop which, by increasing a penalty factor, solves the contact problem to a prescribed tolerance.

2. **Slip damper** This damper object artificially controls the stick-slip behavior of the nodes on the secondary surface. The basic idea is that, by disallowing abrupt changes in the stick-slip behavior of the contacting nodes, the overall system convergence is improved.

These tools have been used with varying degrees success for solving nuclear fuel models using contact. Strategies such as the use of a slip damper and the application of augmented Lagrangian nested solution algorithms have enabled the solution of challenging full-fuel-rod BISON simulations using frictional contact, but significantly add to the computational time. Furthermore, there are a number of fundamental shortcomings of point-wise enforcement. For instance, it is not guaranteed to pass contact patch tests and the solution may exhibit jumps [4]. These aspects of node-on-face enforcement motivated the development of a mortar contact framework that, as analyzed in Section 5, features improved numerical results for realistic case scenarios.

1.2 Mortar formulation

Variational enforcement of contact constraints can be carried out using finite element methods (FEMs) that integrate the constraints over contacting surfaces or segments. Mortar and Nitsche's FEMs are examples of such methods, which can be applied to thermomechanical interactions. In MOOSE and BISON, the ability to generate normal and tangential contact constraints resolved on segments is available for general two-dimensional (2-D) applications, including those featuring plane strain and axisymmetry. Recent progress on mortar contact includes the application of variationally consistent mechanical constraints with dual basis functions (i.e., "dual mortar") to a variety of assessment cases (including smeared and discrete pellets). While there are outstanding tasks regarding the development and generalization of mortar contact, our recent work shows this approach can achieve the expected solution smoothness for relevant 2-D problems.

1.3 Outstanding issues and vision

The current effort was motivated by the fact that there are still a number of outstanding issues with contact enforcement in BISON that limit its ability to solve fuel performance problems, both for current LWRs as well as emerging nuclear reactor designs. Some of the emerging reactor designs are expected to require the solution of significantly more complex contact problems than is currently required in the fuel performance simulations that are routinely performed with BISON. For example, simulation of liquid metal fast reactor (LMFR) core deformation requires enforcement of contact between multiple ducts, and requires three-dimensional (3-D) models. Similarly, microreactor concepts also involve contact between multiple bodies that generally need to be modeled in 3-D.

The issues with the current contact modeling capabiliites in BISON are summarized as follows:

1. **Smoothness** Node/face algorithms have issues with smoothness that affect both the quality of the solutions, as well as the ability to robustly obtain a converged solution. Variationally consistent contact formulations (e.g., mortar FEM) are known to provide smooth evolution of contact forces and temperature. The accurate and consistent creation of mortar segments is key to ensuring smoothness of the contact solution [1].

2. **Scalability** The iterative preconditioning algorithms that are well known to give good scalability for solving large problems do not work well with the existing contact algorithms in MOOSE. As a result, BISON simulations typically use parallel direct solvers, which scale well up to moderately-sized problems ($\sim$100 cpus), but cannot be used for larger problems

because of high memory demands. To solve larger problems, such as those that would be encountered on 3D LWR simulations with more than a few pellets or emerging reactor designs, it is expected that it will be essential to develop approaches to use iterative preconditioning with contact.

3. **Frictional treatment** The nonlinearities introduced by contact constraints become more demanding when adding the stick-slip behavior, due to Coulomb friction. This numerical challenge often causes simulations to fail by the mere addition of frictional tangential mechanical pressure governed by a Coulomb's law. Solution of these problems is significantly more difficult when the contact algorithm gives non-smooth behavior in the computation of the response normal to the surfaces. Additional strategies to improve convergence of frictional mortar constraints may need to be developed.

4. **3-D multibody** Most LWR fuel simulations currently run with BISON are 2-D because of limitations with contact robustness and scalability in 3-D. Additional work is needed to extend the existing 2-D mortar contact formulation to three dimensions and multi-surface contact.

From this general description of necessary enhancements to BISON's contact capabilities, for fiscal year 2021 we focused on the following areas:

1. **Scalability** Enable dual mortar to use iterative solvers (e.g., algebraic multigrid) whose efficiency is relevant for simulating very large problems. The variable condensation preconditioner (VCP) was also developed (see Section 3).

2. **Smoothness** Dual mortar has shown satisfactory results in benchmark problems and assessment cases (see Sections 4 and 5).

3. **Frictional problem** This item is initially addressed within the context of mortar mechanical contact through the implementation of variationally consistent frictional forces. Convergence behavior of frictional problems will be analyzed and their constraint Jacobian improved.

2 Governing equations

We consider the case of two bodies coming into thermomechanical contact. The domains $\Omega^{(\gamma)}$, with $\gamma \in \{1,2\}$ represent two separate bodies. We utilize $\Gamma_c^{(\gamma)}$ to denote the potential contact interface, which is a subset of the boundary $\partial\Omega^{(\gamma)}$. The governing equations for the mechanical and thermal contact are included in the following subsections.

2.1 Mechanical model

To describe the mechanical behavior, the following quasi-static conservation of momentum equation is solved in each subdomain $\Omega^{(\gamma)}$:

$$\begin{aligned} \nabla \cdot \boldsymbol{\sigma}^{(\gamma)} + \boldsymbol{b}^{(\gamma)} &= 0 \qquad \text{in } \Omega^{(\gamma)}, \\ \boldsymbol{u}^{(\gamma)} &= \bar{\boldsymbol{u}}^{(\gamma)} \quad \text{on } \Gamma_u^{(\gamma)}, \\ \boldsymbol{\sigma}^{(\gamma)} \cdot \boldsymbol{n}_t^{(\gamma)} &= \bar{\boldsymbol{t}}^{(\gamma)} \quad \text{on } \Gamma_t^{(\gamma)}, \end{aligned} \tag{1}$$

where $\boldsymbol{\sigma}^{(\gamma)}$ is the Cauchy stress tensor, $\boldsymbol{u}^{(\gamma)}$ is the displacement vector, $\boldsymbol{b}^{(\gamma)}$ is the body force, $\boldsymbol{n}_t^{(\gamma)}$ is the unit normal to the traction boundary, $\bar{\boldsymbol{u}}^{(\gamma)}$ is the prescribed displacement boundary condition,

and $\bar{\boldsymbol{t}}^{(\gamma)}$ is the prescribed traction boundary condition. The displacement, traction, and contact boundaries are disjoint from each other (i.e., $\Gamma_u^{(\gamma)} \cap \Gamma_t^{(\gamma)} = \Gamma_t^{(\gamma)} \cap \Gamma_c^{(\gamma)} = \Gamma_u^{(\gamma)} \cap \Gamma_c^{(\gamma)} = \varnothing$).

The contact constraints are defined on $\Gamma_c^{(1)}$ as:

$$\begin{aligned} &g_n \geq 0,\ p_n \leq 0,\ p_n g_n = 0, \\ &\Phi := ||\boldsymbol{t}_\tau|| - \mu |p_n| \leq 0, \\ &\boldsymbol{v}_{\tau,\text{rel}} + \beta \boldsymbol{t}_\tau = \boldsymbol{0},\ \beta \geq 0,\ \Phi\beta = 0. \end{aligned} \tag{2}$$

Here, g_n is the gap function that measures the proximity of the two bodies, such that:

$$g_n = -\boldsymbol{n}^{(1)} \cdot \left(\boldsymbol{x}^{(1)} - \mathcal{P}\boldsymbol{x}^{(2)} \right), \tag{3}$$

where $\mathcal{P}$ represents a projection of variables from the mortar to the non-mortar side and $\boldsymbol{n}^{(1)}$ denotes the outward unit normal on the non-mortar surface. μ is the friction coefficient, $\boldsymbol{v}_{\tau,\text{rel}}$ is the relative tangential velocity, $\boldsymbol{t}_\tau$ is the tangential contact force, and p_n denotes the contribution of the contact traction along the normal direction. The contact traction can thus be decomposed into normal and tangential parts as $\boldsymbol{t}_c^{(1)} = p_n \boldsymbol{n}^{(1)} + \boldsymbol{t}_\tau$, where $\boldsymbol{t}_\tau$ is the tangential contact force. For more details on this mechanical contact constraint, refer to [8].

The balance of the linear momentum at the contact interface is typically enforced by introducing a Lagrange multiplier vector $\boldsymbol{\lambda}$. For mechanical contact, $\boldsymbol{\lambda} = -\boldsymbol{t}_c^{(1)}$ represents the negative contact traction on the non-mortar side. The weak (integral) form of the mechanical model is expressed as:

$$\begin{aligned} \sum_{\gamma=1}^{2} \Bigg\{ &\int_{\Omega^{(\gamma)}} \left(\delta\boldsymbol{\varepsilon}^{(\gamma)} : \boldsymbol{\sigma}^{(\gamma)} \right) \, \mathrm{d}\Omega - \int_{\Omega^{(\gamma)}} \boldsymbol{b}^{(\gamma)} \cdot \delta\boldsymbol{u}^{(\gamma)} \, \mathrm{d}\Omega \\ &- \int_{\Gamma_t^{(\gamma)}} \left(\bar{\boldsymbol{t}}^{(\gamma)} \cdot \delta\boldsymbol{u}^{(\gamma)} \right) \, \mathrm{d}s \Bigg\} \\ &+ \int_{\Gamma_c^{(1)}} \boldsymbol{\lambda} \left(\delta\boldsymbol{u}^{(1)} - \mathcal{P}\delta\boldsymbol{u}^{(2)} \right) \, \mathrm{d}s = 0, \end{aligned} \tag{4}$$

supplemented by (see [8]):

$$\int_{\Gamma_c^{(1)}} \left(\delta\lambda_n - \lambda_n \right) g_n \, \mathrm{d}s \geq 0 \text{ and } \int_{\Gamma_c^{(1)}} \left(\delta\boldsymbol{\lambda}_\tau - \boldsymbol{\lambda}_\tau \right) \cdot \boldsymbol{v}_{\tau,\text{rel}} \, \mathrm{d}s \geq 0. \tag{5}$$

Here, λ_n is the normal contribution of $\boldsymbol{\lambda}$. λ_n and $\boldsymbol{\lambda}_\tau$ are the normal and tangential contributions of $\boldsymbol{\lambda}$, respectively.

The integral form of frictional mortar constraints is:

$$\int_{\Gamma_c^{(1)}} (\lambda_m \delta g_n + \delta\lambda_m + \boldsymbol{t}_\tau \cdot \delta\boldsymbol{g_\tau}) \mathrm{d}\Gamma_c^{(1)}, \tag{6}$$

where λ_m is a mechanical contact Lagrange multiplier, g_n is the contact gap, δ denotes the variational operator, $\boldsymbol{t}_\tau$ is the tangential pressure, $\boldsymbol{g}_\tau$ is the tangential distance, and $\Gamma_c^{(1)}$ is the non-mortar contact surface where the contact constraints are enforced [15].

2.2 Thermal model

To describe the thermal behavior, the heat conduction equation is solved in two bodies:

$$\begin{aligned} \rho^{(\gamma)} c^{(\gamma)} \frac{\partial T^{(\gamma)}}{\partial t} &= \nabla \kappa^{(\gamma)} \nabla T^{(\gamma)} + f^{(\gamma)}, \text{ in } \Omega^{(\gamma)} \\ T^{(\gamma)} &= \bar{T}^{(\gamma)}, \text{ on } \Gamma_T^{(\gamma)} \\ -\kappa^{(\gamma)} \nabla T^{(\gamma)} \cdot \boldsymbol{n}_q^{(\gamma)} &= \bar{q}^{(\gamma)}, \text{ on } \Gamma_q^{(\gamma)} \end{aligned} \tag{7}$$

where $\rho^{(\gamma)}$ is the density, $c^{(\gamma)}$ is the specific heat, $\kappa^{(\gamma)}$ is the thermal conductivity, $T^{(\gamma)}$ is the temperature variable, $\boldsymbol{n}_q^{(\gamma)}$ is the unit normal to the flux boundary, $f^{(\gamma)}$ is a heat source, $\bar{T}^{(\gamma)}$ is the prescribed temperature boundary condition, and $\bar{q}^{(\gamma)}$ is the prescribed heat flux boundary condition. Again, the temperature, heat flux, and contact boundaries are non-overlapping (i.e., $\Gamma_T^{(\gamma)} \cap \Gamma_q^{(\gamma)} = \Gamma_q^{(\gamma)} \cap \Gamma_c^{(\gamma)} = \Gamma_T^{(\gamma)} \cap \Gamma_c^{(\gamma)} = \emptyset$).

When the two bodies come into contact (i.e., $g_n = 0, p_n \leq 0$ in Equation (2)), we consider heat transfer phenomena between the two material bodies. Under the assumption of no frictional dissipation or energy stored on $\Gamma_c^{(\gamma)}$, the heat flux can be described as:

$$\begin{aligned} q_c^{(1)} &= h(T^{(1)} - T^{(2)}) \text{ on } \Gamma_c^{(1)}, \\ q_c^{(2)} &= h(T^{(2)} - T^{(1)}) \text{ on } \Gamma_c^{(2)}, \end{aligned} \tag{8}$$

where h is a heat transfer coefficient.

The weak formulation for the thermal contact problem can be written in a compact form by introducing an additional Lagrange multiplier variable [12] to represent the heat flux:

$$\lambda_T = q_c^{(1)} = -q_c^{(2)}. \tag{9}$$

The weak formulation for the heat conduction in two contacting bodies is as follows:

$$\begin{aligned} \sum_{\gamma=1}^{2} \Bigg\{ & \int_{\Omega^{(\gamma)}} \left(\rho^{(\gamma)} c^{(\gamma)} \frac{\partial T^{(\gamma)}}{\partial t} \right) \delta T^{(\gamma)} \, \mathrm{d}\Omega + \\ & \int_{\Omega^{(\gamma)}} \left(k^{(\gamma)} \nabla T^{(\gamma)} \cdot \nabla \delta T^{(\gamma)} - f^{(\gamma)} \delta T^{(\gamma)} \right) \, \mathrm{d}\Omega + \\ & \int_{\Gamma_q^{(\gamma)}} \bar{q}^{(\gamma)} \delta T^{(\gamma)} \, \mathrm{d}s \Bigg\} + \int_{\Gamma_c^{(1)}} \lambda_T \left(\delta T^{(1)} - \mathcal{P} \delta T^{(2)} \right) \, \mathrm{d}s = 0 \end{aligned} \tag{10}$$

and

$$\int_{\Gamma_C^{(1)}} \left[\lambda_T - h \left(T^{(1)} - \mathcal{P} T^{(2)} \right) \right] \delta \lambda_T \, \mathrm{d}s = 0. \tag{11}$$

The operator $\mathcal{P}$ (see Equation (3)) projects the primal variable from the mortar side to the non-mortar side.

2.3 Finite element discretization

There are two common approaches to discretizing the mortar Lagrange multipliers: the standard approach and the dual approach. The standard approach leads to a combination of shape functions that must satisfy the *inf-sup* condition. In contrast, the dual approach constructs dual Lagrange multiplier shape functions, based on a biorthogonal condition with the primal variable shape functions.

The standard finite element interpolation is employed to approximate the primal variables $\boldsymbol{u}(\boldsymbol{x})$ and $T(\boldsymbol{x})$:

$$\begin{aligned} \boldsymbol{u}(\boldsymbol{x}) &\approx \sum_{k=1}^{n_u} \phi_u^{(k)}(\boldsymbol{x}) \mathbf{u}^{(k)}, \\ T(\boldsymbol{x}) &\approx \sum_{k=1}^{n_T} \phi_T^{(k)}(\boldsymbol{x}) \mathbf{T}^{(k)}, \end{aligned} \tag{12}$$

where n_u and n_T represent the number of DoFs of u and T, respectively. $\mathbf{u}^{(k)}$ and $\mathbf{T}^{(k)}$ denote the nodal discrete variables. $\phi_u^{(k)}(\boldsymbol{x})$ and $\phi_T^{(k)}(\boldsymbol{x})$ are the standard shape functions.

The Lagrange multipliers λ and λ_T are approximated by:

$$\begin{aligned} \lambda(\boldsymbol{x}) &\approx \sum_{k=1}^{n_\lambda} \psi^{(k)}(\boldsymbol{x}) \boldsymbol{\lambda}^{(k)}, \\ \lambda_T(\boldsymbol{x}) &\approx \sum_{k=1}^{n_{\lambda_T}} \psi_T^{(k)}(\boldsymbol{x}) \boldsymbol{\lambda}_T^{(k)}, \end{aligned} \tag{13}$$

where n_λ and n_{λ_T} represent the number of DoFs of λ and λ_T, respectively. $\boldsymbol{\lambda}^{(k)}$ and $\boldsymbol{\lambda}_T^{(k)}$ denote the nodal discrete values. $\psi^{(k)}(\boldsymbol{x})$ and $\psi_T^{(k)}(\boldsymbol{x})$ are the basis functions.

In this work, the shape function $\psi^{(k)}(\boldsymbol{x})$ takes the form of a dual basis function, fulfilling the following biorthogonal condition along the contact interface $\Gamma_c^{(1)}$:

$$\int_{\Gamma_c^{(1)}} \psi^{(j)}(\boldsymbol{x}) \phi^{(k)}(\boldsymbol{x}) \, \mathrm{d}s = \delta_{jk} \int_{\Gamma_c^{(1)}} \phi^{(k)}(\boldsymbol{x}) \, \mathrm{d}s, \tag{14}$$

where δ_{jk} is the Kronecker delta function. There are many possible choices of dual basis function that satisfy Equation (14). The interested reader is referred to Ref. [14].

In our study, the dual basis functions are assumed to be linear combinations of the standard finite element shape functions:

$$\psi_j(\boldsymbol{x}) = \sum_{j=1}^{n_{e,\lambda}} a_{kj} \phi_k(\boldsymbol{x}), \tag{15}$$

where $n_{e,\lambda}$ is the number of DoFs of the Lagrange multiplier in the lower-dimensional element and a_{jk} denotes the undetermined coefficients. One can obtain a_{jk} by substituting Equation (15) into the biorthogonal condition (i.e., Equation (14)) and solving the resultant local system of equations.

Next, we focus on discretization of the contact constraints. The discretized version of the mechanical contact constraint in Equation (2) is equivalent to the following conditions [8]:

$$\begin{aligned} \left(\tilde{g}_n\right)_j \geq 0, \ \left(\lambda_n\right)_j \geq 0, \ \left(\tilde{g}_n\right)_j \left(\lambda_n\right)_j = 0, \\ \Phi_j := \left|\left| \left(\boldsymbol{\lambda}_\tau\right)_j \right|\right| - \mu \left| \left(\lambda_n\right)_j \right| \leq 0, \\ \left(\tilde{\boldsymbol{v}}_{\tau,\mathrm{rel}}\right)_j + \beta_i \left(\boldsymbol{\lambda}_\tau\right)_j = \mathbf{0}, \ \beta_j \geq 0, \ \Phi_j \beta_j = 0, \end{aligned} \tag{16}$$

where $j = 1 \ldots n_\lambda$. $\left(\tilde{g}_n\right)_j$ is the discrete weighted gap and $\left(\tilde{\boldsymbol{v}}_{\tau,\mathrm{rel}}\right)_j$ is the discrete weighted relative tangential velocity vector at the non-mortar node j. Specifically:

$$\begin{aligned} \left(\tilde{g}_n\right)_j &= \int_{\Gamma_c^{(1)}} \psi_j g_n \, \mathrm{d}s, \\ \left(\tilde{\boldsymbol{v}}_{\tau,\mathrm{rel}}\right)_j &= \int_{\Gamma_c^{(1)}} \psi_j \mathbf{v}_{\tau,\mathrm{rel}} \, \mathrm{d}s. \end{aligned} \tag{17}$$

Equations (16) and (17) represent a variationally consistent discrete formulation of the original mechanical contact constraint (see Equation (2)), with an additional weighting based on the Lagrange multiplier shape functions [6, 8].

Computation of the mortar integrals relies on gap functions that depend on primal variables and can lead to inaccuracies if proper care is not taken. A numerical analysis on the computation of mortar integrals and projection matrices can be found in [5].

2.4 Code implementation

The formulation presented in Section 2.3 has benefited from various implementation improvements:

- **Contact constraint equations** A variationally consistent formulation of normal and friction contact constraints [14] is followed. The constraints use weak ("weighted") contact quantities, such as normal gap and tangential velocities. The frictional constraints are expressed mathematically such that it can distinguish between nodes in contact, slipping, and sticking, in a primal-dual active set strategy (see [3]).
- **Consistency in mortar segment creation** To improve the consistency of the geometric definition of mortar segments, normal vector fields from the secondary (non-mortar) surface are now employed for projecting both the primary and secondary surface's nodes. A detailed description of how mortar segments are generated is given in [5]. Additionally, minor tune-ups to the generation of segments enabled simulations of new problems.
- **Normal vector field in contact constraints** Instead of the non-smooth normal vectors to the element faces, the normal field from the mortar segments is now used in the contact constraints.
- **Computation of dual basis functions** The quadrature rule used to compute dual coefficients was improved. This allows for simulating second-order meshes and second-order dual Lagrange multipliers with improved convergence behavior.

• 3 Dual mortar and preconditioner

The addition of the dual mortar capability offers three major advantages: (1) removing the numerical instability often encountered in the standard mortar approach [10] (see Sections 4 and 5); (2) reducing the number of nonlinear and linear iterations, thus improving the overall convergence (see Section 4); (3) allowing for static condensation of the Lagrange multipliers, which restores the positive definiteness of the system matrix and thus improves the scaling property by enabling usage of a broader range of robust preconditioners/solvers.

During FY20, we demonstrated the potential of this approach by solving a simple diffusion problem with equal value constraint (see FY20 progress in [9]). For FY21, we extended this capability, successfully applying dual mortar to more complicated problems (e.g., mortar-based thermal contact, mechanical contact, and thermomechanical contact) in BISON.

3.1 Dual mortar for contact

The typical saddle point structure (e.g., zero diagonal entries in a Jacobian matrix) associated with mortar-based contact problems prevents usage of a wide range of robust itera-

tive solvers and preconditioners. Using the dual basis function simplifies the mortar matrix that represents the coupling between the primal variable (e.g., displacements or temperature) and the corresponding Lagrange multiplier. This enables static condensation of the Lagrange multipliers with minimal computation, restoring a positive definite system that can be solved efficiently using robust iterative solvers.

Note that the saddle point structure comes from the mechanical contact formulation, in which the Lagrange multiplier (λ) is not coupled with its own test function (see Equations (5) and (6)). For thermal contact, the weak formulation of the thermal constraint (see Equation (11)) has a coupling term between the thermal Lagrange multiplier (λ_T) and its own test function. This indicates that no saddle point will result from the thermal contact constraints, regardless of basis function type. Therefore, thermal contact generally does not add to the complexity for dual mortar in terms of the static condensation step for avoiding a saddle point structure. Therefore, in this subsection, we will focus our discussion on mechanical contact.

After the finite element discretization (see Section 2.3), we can write out the block-wise Jacobian matrix of a mortar-based mechanical contact problem as follows:

$$\begin{bmatrix} \boldsymbol{K}_{\omega\omega} & \boldsymbol{K}_{\omega m} & \boldsymbol{K}_{\omega i} & \boldsymbol{K}_{\omega a} & 0 & 0 \\ \boldsymbol{K}_{m\omega} & \boldsymbol{K}_{mm} & \boldsymbol{K}_{mi} & \boldsymbol{K}_{ma} & -\boldsymbol{M}_i^{\mathsf{T}} & -\boldsymbol{M}_a^{\mathsf{T}} \\ \boldsymbol{K}_{i\omega} & \boldsymbol{K}_{im} & \boldsymbol{K}_{ii} & \boldsymbol{K}_{ia} & \boldsymbol{D}_i & 0 \\ \boldsymbol{K}_{a\omega} & \boldsymbol{K}_{am} & \boldsymbol{K}_{ai} & \boldsymbol{K}_{aa} & 0 & \boldsymbol{D}_a \\ 0 & 0 & 0 & 0 & \boldsymbol{I}_i & 0 \\ 0 & \widetilde{\boldsymbol{M}}_a & \boldsymbol{S}_{ai} & \boldsymbol{S}_{aa} & 0 & 0 \\ 0 & 0 & \boldsymbol{F}_{ai} & \boldsymbol{F}_{aa} & 0 & \boldsymbol{T}_a \end{bmatrix} \begin{bmatrix} \Delta\boldsymbol{u}_\omega \\ \Delta\boldsymbol{u}_m \\ \Delta\boldsymbol{u}_i \\ \Delta\boldsymbol{u}_a \\ \Delta\boldsymbol{\lambda}_i \\ \Delta\boldsymbol{\lambda}_a \end{bmatrix} = \begin{bmatrix} \Delta\boldsymbol{r}_\omega \\ \Delta\boldsymbol{r}_m \\ \Delta\boldsymbol{r}_i \\ \Delta\boldsymbol{r}_a \\ 0 \\ \Delta\boldsymbol{g}_a \\ 0 \end{bmatrix}, \tag{18}$$

where the right-hand side denotes the change in the residual, due to contact. $\boldsymbol{g}$ contains the residual entries associated with a weighted gap. $\boldsymbol{u}$ denotes the vector of displacement DoFs, and $\boldsymbol{\lambda}$ denotes the vector of the Lagrange multiplier. The subscripts m, i, a, and ω indicate the mortar side, the inactive non-mortar side, the active non-mortar side, and the rest of the domain, respectively.

With the use of dual shape functions, the mortar integral matrix

$$\boldsymbol{D} = \begin{bmatrix} \boldsymbol{D}_i & 0 \\ 0 & \boldsymbol{D}_a \end{bmatrix} \tag{19}$$

becomes diagonal, thus the discrete Lagrange multipliers can be eliminated via static condensation at negligible computational cost:

$$\Delta\boldsymbol{\lambda} = \boldsymbol{D}^{-1} \left(\Delta\boldsymbol{r}_n - \boldsymbol{K}_{n\omega}\Delta\boldsymbol{u}_\omega - \boldsymbol{K}_{nm}\Delta\boldsymbol{u}_m - \boldsymbol{K}_{nn}\Delta\boldsymbol{u}_n \right), \tag{20}$$

where the subscript n denotes the non-mortar side that includes both the inactive and active contributions, such that:

$$\begin{gathered} \Delta\boldsymbol{\lambda} = \begin{bmatrix} \Delta\boldsymbol{\lambda}_i \\ \Delta\boldsymbol{\lambda}_a \end{bmatrix}, \ \Delta\boldsymbol{r}_n = \begin{bmatrix} \Delta\boldsymbol{r}_i \\ \Delta\boldsymbol{r}_a \end{bmatrix}, \\ \boldsymbol{K}_{n\omega} = \begin{bmatrix} \boldsymbol{K}_{i\omega} \\ \boldsymbol{K}_{a\omega} \end{bmatrix}, \ \boldsymbol{K}_{nm} = \begin{bmatrix} \boldsymbol{K}_{im} \\ \boldsymbol{K}_{am} \end{bmatrix}, \ \boldsymbol{K}_{nn} = \begin{bmatrix} \boldsymbol{K}_{ii} & \boldsymbol{K}_{ia} \\ \boldsymbol{K}_{ai} & \boldsymbol{K}_{aa} \end{bmatrix}. \end{gathered} \tag{21}$$

This ensures that the final linear system of equations contains only the displacement DoFs:

$$\begin{bmatrix} \boldsymbol{K}_{\omega\omega} & \boldsymbol{K}_{\omega m} & \boldsymbol{K}_{\omega i} & \boldsymbol{K}_{\omega a} \\ \boldsymbol{K}_{m\omega} + \widehat{\boldsymbol{M}}_a^{\intercal} \boldsymbol{K}_{a\omega} & \boldsymbol{K}_{mm} + \widehat{\boldsymbol{M}}_a^{\intercal} \boldsymbol{K}_{am} & \boldsymbol{K}_{mi} + \widehat{\boldsymbol{M}}_a^{\intercal} \boldsymbol{K}_{ai} & \boldsymbol{K}_{ma} + \widehat{\boldsymbol{M}}_a^{\intercal} \boldsymbol{K}_{aa} \\ \boldsymbol{K}_{i\omega} & \boldsymbol{K}_{im} & \boldsymbol{K}_{ii} & \boldsymbol{K}_{ia} \\ 0 & \widetilde{\boldsymbol{M}}_a & \boldsymbol{S}_{ai} & \boldsymbol{S}_{aa} \\ \boldsymbol{T}_a \boldsymbol{D}_a^{-1} \boldsymbol{K}_{a\omega} & \boldsymbol{T}_a \boldsymbol{D}_a^{-1} \boldsymbol{K}_{am} & \boldsymbol{T}_a \boldsymbol{D}_a^{-1} \boldsymbol{K}_{ai} - \boldsymbol{F}_{ai} & \boldsymbol{T}_a \boldsymbol{D}_a^{-1} \boldsymbol{K}_{aa} - \boldsymbol{F}_{aa} \end{bmatrix} \cdot \begin{bmatrix} \Delta \boldsymbol{u}_\omega \\ \Delta \boldsymbol{u}_m \\ \Delta \boldsymbol{u}_i \\ \Delta \boldsymbol{u}_a \end{bmatrix} = \begin{bmatrix} \Delta \boldsymbol{r}_\omega \\ \Delta \boldsymbol{r}_m + \widehat{\boldsymbol{M}}_a^{\intercal} \Delta \boldsymbol{r}_a \\ \Delta \boldsymbol{r}_i \\ \Delta \boldsymbol{g}_a \\ \boldsymbol{T}_a \boldsymbol{D}_a^{-1} \Delta \boldsymbol{r}_a \end{bmatrix}, \tag{22}$$

where we have $\widehat{\boldsymbol{M}}_a = \boldsymbol{D}_a^{-1} \boldsymbol{M}_a$. Since the resulting system is positive definite, iterative solvers such as multigrid methods are applicable. Once the displacement DoFs are obtained, the Lagrange multipliers ($\Delta \boldsymbol{\lambda}$) can be recovered from the displacements via Equation (20).

3.2 Variable condensation preconditioner

To carry out static condensation of the Lagrange multipliers and apply iterative solvers/preconditioners to the resultant system of equations, we developed a new preconditioner type (i.e., VCP) based on the MOOSE framework. A schematic is included in Figure 1 to demonstrate the solution process of VCP. Compared to the standard precondition and solve procedure, VCP features two additional customized computation steps (i.e., one to condense out the variable and the other to obtain the full solution vector) (see Figure 1). During static condensation of the variable (e.g., λ), the DoFs are obtained for both the variable itself (λ) and its coupled variable (u). Based on this information, the mortar matrices (i.e., $\boldsymbol{D}$ and $\boldsymbol{M}$) will be extracted from the original Jacobian matrix. Then a reduced system of equations will be obtained with the necessary submatrix operations following Equation (22). After solving the reduced system of equations, we obtain the primal variable solution vector, which is then utilized to update the variable λ (see Equation (20)) and assemble the full solution vector.

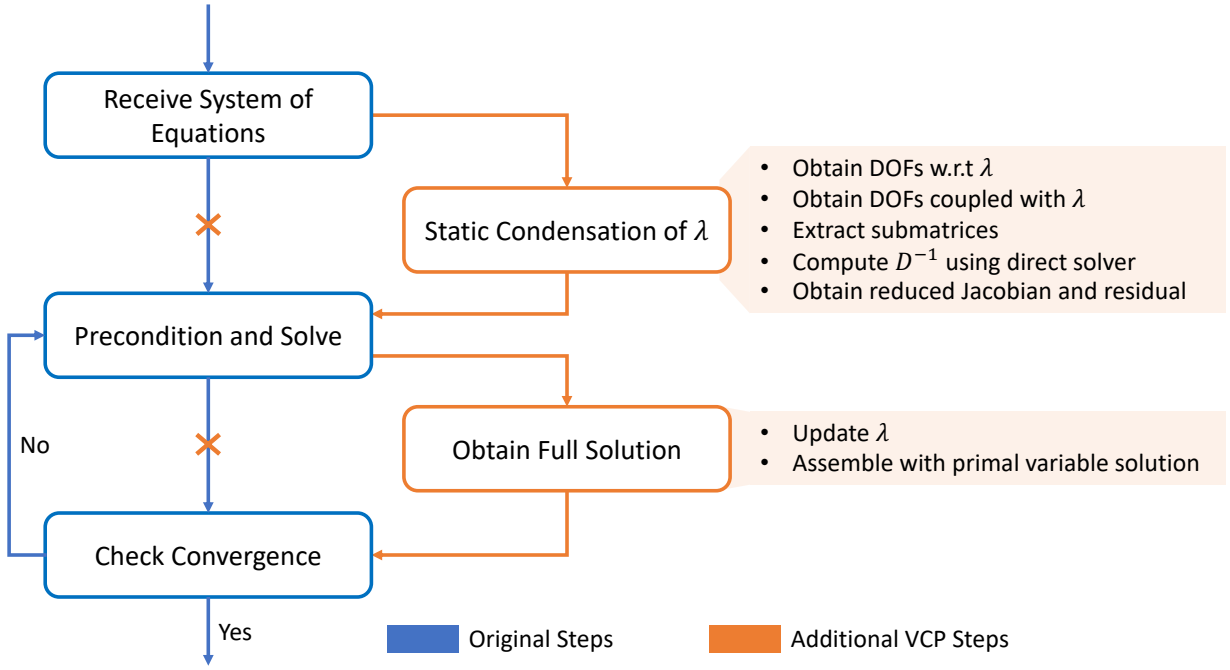

Figure 1: VCP workflow. Blue represents the original preconditioning steps. Orange shows the additional steps customized for VCP.

Several special designs in VCP foster improved performance. First, we have an adaptive variable condensation mechanism. The idea is to obtain the actual DoFs that have zero diagonal entries by checking the Jacobian matrix at runtime. This refines the DoF list such that variable condensation will only be carried out for those DoFs that result in a saddle point structure, and will only happen when the bodies come into contact. Second, VCP is designed to work with both standard and dual basis formulations. If dual bases are utilized, the mortar matrix $\boldsymbol{D}$ is strictly diagonal. If standard bases are utilized, $\boldsymbol{D}$ has off-diagonal entries. During the computation of $\boldsymbol{D}^{-1}$, when $\boldsymbol{D}$ is diagonal, inversion is trivial to obtain. When $\boldsymbol{D}$ is not strictly diagonal, the user can choose to either use an LU solver or obtain an approximated inverse using the diagonal entries. Third, although we are focused on using VCP for mortar-based contact problems with a saddle point structure, VCP was developed to be applicable to general problems in which improved conditioning is achievable via a reduced number of DoFs.

In addition to developing VCP following literature descriptions (see Section 3.1) that are aimed at solving mechanical contact problems, we made an initial attempt to apply VCP to the more complicated BISON problems. Several issues were revealed in this process and motivated special designs to address them. First, a limitation in the condensation step (see Equation (22)) is removed. Note the Equations (18) and (22) describe the system matrix and the condensation step for a typical mortar-based mechanical contact problem. BISON problems are often multiphysics in nature thus demonstrate sparsity patterns that are different from what is described in Equation (18). In order to apply VCP to BISON problems, a more general condensation step is needed. To address this issue, changes have been made in VCP to eliminate assumptions about the sparsity of the system matrix. Specifically, during variable condensation, more DoFs are accounted for in the mortar matrix ($\boldsymbol{M}$). Instead of accounting for only the DoFs of the displacement variable on the primary surface, the rows

of $\boldsymbol{M}$ correspond to all but the DoFs from the Lagrange multipliers. This enables the VCP to converge for more complicated multiphysics BISON cases (see Section 5.3). Meanwhile, we note that expanding $\boldsymbol{M}$ can make the condensation step more expensive than described in Equation (22), in terms of both memory and computation costs. Second, improvements are made in the initialization and the computation of the condensed system. Initial code profiling reveals a heavy overhead while allocating memory for the condensed system of equations. Therefore, memory estimation and pre-allocation have been developed in VCP for improved efficiency. Indexing of the DoFs was made more efficient by switching from searching in vectors to using unordered maps. Moreover, a specialized one-step calculation of the reduced system of equations is implemented in place of the original multi-step computation, which further improves the efficiency by avoiding the frequent matrix finalization operations that are costly in the multi-step approach. All the above improvements in VCP will be demonstrated later in Sections 4.1 and 5.3.

3.3 VCP for thermomechanical contact

During FY20, we tested the mortar implementation of the LWR gap conductance model by demonstrating a problem with two blocks coming into mechanical and thermal contact [9]. With the newly developed VCP, along with dual mortar, we can solve this problem using the algebraic multigrid method (e.g., BoomerAMG) as a sub-preconditioner embedded in VCP.

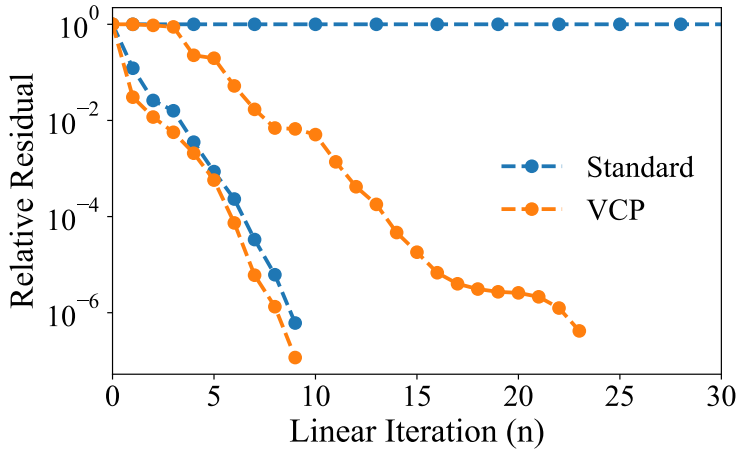

Figure 2: Relative residual value as a function of the linear iteration count during a typical linear solve. Both the standard and VCP approaches are shown with BoomerAMG as the preconditioner. The two curves on the bottom left correspond to a time step before contact. The two curves on the right correspond to a time step after coming into contact.

Figure 2 shows the relative residual values as a function of the linear iteration count during a typical linear solve. Here, we utilize BoomerAMG as the preconditioner. For the standard approach, we apply the preconditioner to the entire problem. For the VCP approach, the preconditioner is applied on the condensed problem. We show the relative residual change at two different time steps, one before coming into contact, the other after coming into contact. It can be seen that VCP converges well both before and after the two bodies come into contact. During contact, VCP requires an increased number of linear iterations, indicating that the system of linear equations becomes numerically more challenging to solve. Before

contact, the standard approach converges at a rate similar to that of VCP; however, the solver stagnates due to the saddle point structure during contact.

Here, we demonstrate successful application of VCP to a thermomechanical contact problem in BISON. However, enhancing the robustness of VCP, making it applicable to extensive mortar-based contact problems with increased complexity (e.g., those shown in Sections 5.2.1 and 5.2.2), and obtaining an optimal scaling property will require additional effort throughout the rest of FY21.

4 Mechanical contact benchmark problems

This section outlines the numerical results of two benchmark problems commonly used by the contact mechanics community to examine algorithmic robustness and correctness. For each problem, we compare the performance between the node-on-face and mortar formulations. To demonstrate the benefits achieved by recent progress, we show the results for both the standard mortar and dual mortar approaches. Here, "standard mortar" refers to using the standard basis function, while "dual mortar" refers to using the dual basis function. In both cases, solution fields are plotted using linear interpolations. Additional post-processing steps using other interpolation functions may demonstrate solution characteristics that are different from what is shown in this report, and are beyond the scope of this report.

4.1 Hertzian contact (cylinder on a plane)

Here, we present the numerical results of a 2-D Hertzian-type contact for a cylindrical body with a rigid planar surface under plane-strain conditions. The problem setting is shown in Figure 3. The horizontal upper boundary of the half cylinder undergoes a linearly increasing vertical displacement $\bar{u}_y$ until the maximum displacement of 0.2 is reached in 2 seconds. We assume finite strain elastic behavior in both the cylinder and the block, with the cylinder having an elastic modulus of 1 MPa and a Poisson's ratio of 0.3, and the block having an elastic modulus of 1000 MPa and a Poisson's ratio of 0.3.

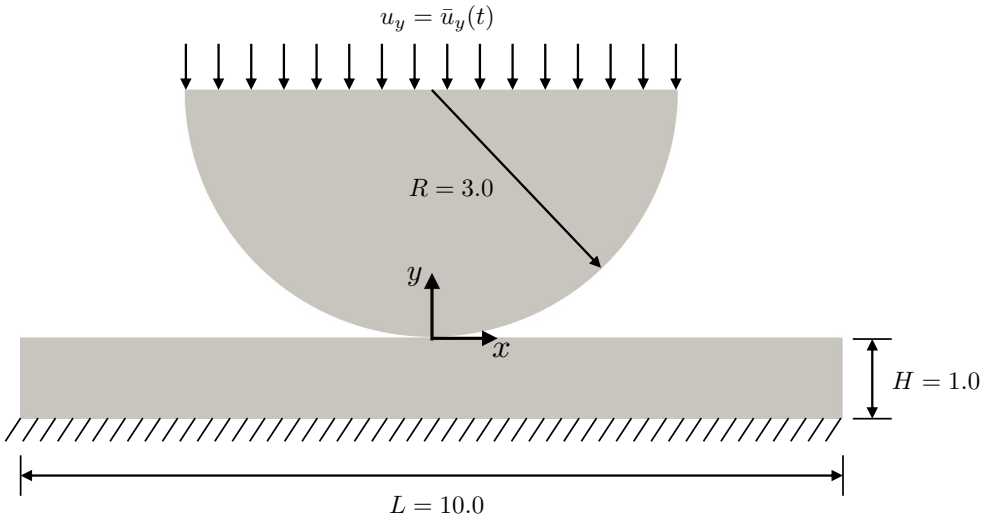

Figure 3: Cylinder on a plane problem setting in 2-D. Only half the cylinder is simulated, due to the symmetric geometry. A Dirichlet boundary condition is applied on the top surface of the half cylinder.

As an illustration, this problem is solved using both the node-on-face and mortar approaches. The mortar results are based on the recent weighted gap implementation in the contact constraints, as per Equations (16) and (17). In Figure 4, snapshots of the stress field (σ_{yy}) are shown at two different time steps, indicating an increased magnitude of overall stress with increased deformation.

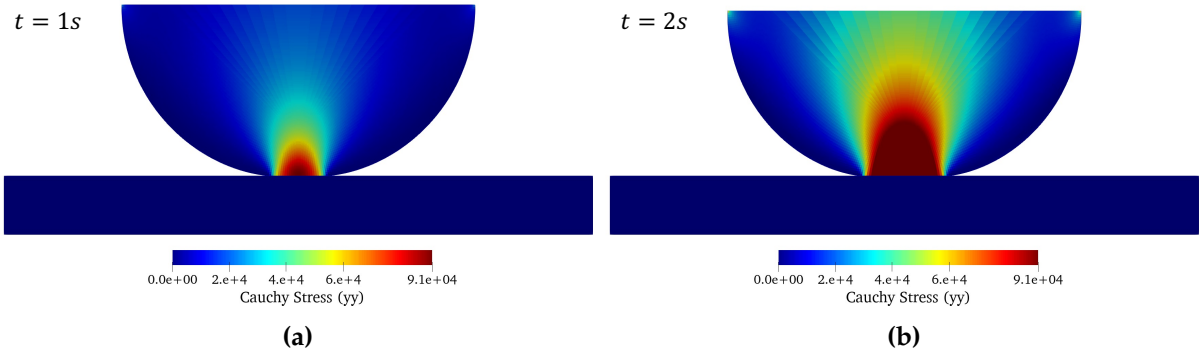

Figure 4: Stress fields at two different time steps. The magnitude of stress increases with larger compression. The absolute value of the y directional Cauchy stress (σ_{yy}) is shown for both cases.

The contact pressure values on the one-dimensional contact interface are plotted in Figure 5. The contact pressure is shown for both the node-on-face and mortar (standard and dual) contact formulations using different order of the basis functions (i.e., first order, second order, and mixed order) on both a coarse and a refined mesh. Figure 5 shows excellent agreement between the existing node-on-segment approach and the mortar finite element approach using dual basis functions for the Lagrange multipliers. Meanwhile, the standard mortar approach introduces some artificial oscillations, especially when the surfaces coming into mechanical contact are not perfectly flat. This effect is especially prominent on a coarse mesh (see Figures 5a and 5b). Refining the mesh can reduce the oscillations (see Figures 5c

and 5d), but not completely eliminate them. On the other hand, use of dual Lagrange multipliers (dual mortar approach) can reduce/eliminate this effect. The instabilities produced by the standard mortar approach at the boundaries of the contact zone are posited to be a result of the localized active set strategy, as pointed out in [10]: the consistent decoupling of contact constraints is only achieved via the dual basis, which eliminates the possibility of an imbalance between virtual work contributions and the discretized mortar constraints.

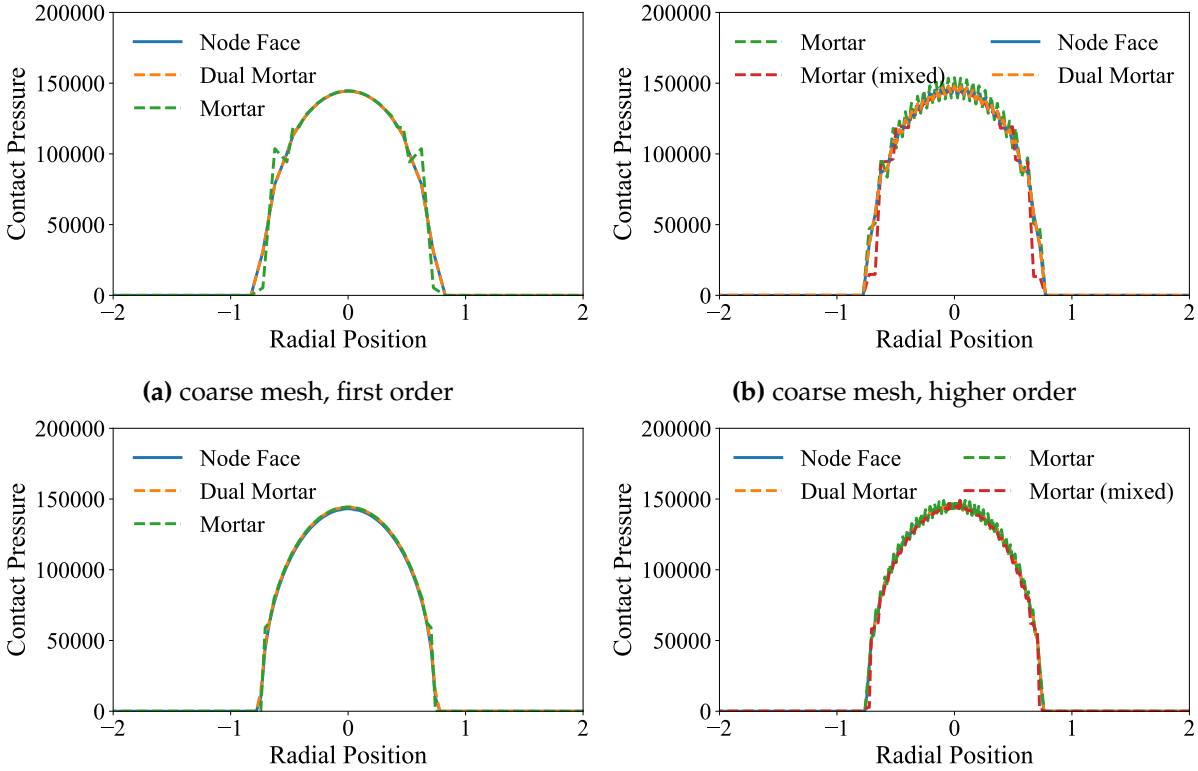

(a) coarse mesh, first order

(b) coarse mesh, higher order

(c) fine mesh, first order

(d) fine mesh, higher order

Figure 5: Comparison of contact pressure results using node-on-face, dual, and standard mortar approaches. Results are shown for two meshes (i.e., a coarse mesh [a-b] and a fine mesh [c-d]). (a, c) Results using first-order approximation. (b, d) Results using second-order approximation (and mixed formulation for standard mortar). This simple problem highlights that dual bases eliminates the solution instabilities caused by a standard mortar approach.

In addition, the dual mortar approach represents a turnaround advantage. To demonstrate this, we summarize the total time steps, linear/nonlinear iterations, and wall time for all three formulations, using different order of interpolations (see Figure 6). Since we focus on comparing different contact formulations, we use LU as the linear solver for all cases. Proper time step sizes are chosen in order to minimize the number of failed solve while reducing the total number of time steps. For the same interpolation order, the total number of time steps among different methods are the same. The standard mortar approach requires the most linear and nonlinear iterations among the three approaches. The dual mortar approach requires slightly more linear and nonlinear iterations than the node-on-face approach, but outperforms both node-on-face and standard mortar in terms of the total wall time. The better performance of dual mortar can be explained by the faster linear/nonlinear solve,

which is a result of the simplified coupling of the contact constraints in the integral form (see Equation (14)).

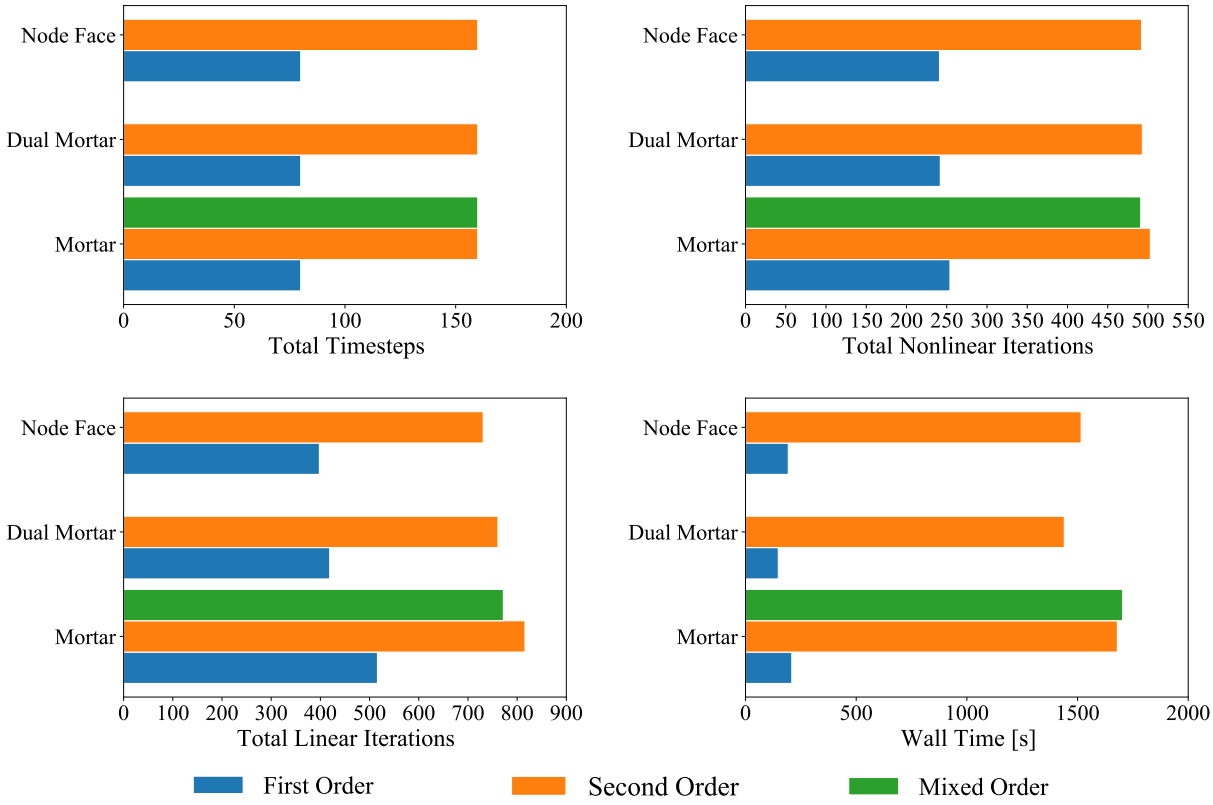

Figure 6: Performance results for the Hertzian problem. Three contact formulations (i.e., node-on-face, dual mortar, and standard mortar) are compared. Different combinations of the basis functions are utilized.

As described in Section 3.2, we developed a new preconditioner type (i.e., VCP) for condensing out the Lagrange multipliers and thus enabling the use of a variety of iterative preconditioners for mortar-based contact problems. As an illustration, we solve this Hertzian problem by using VCP with several sub-preconditioner types, including boomerAMG (AMG), successive over-relaxation (SOR), additive Schwarz method (ASM), and block Jacobi (BJAC). Note that here, ASM, and BJAC converge for the mortar-based mechanical contact problem, both as a standalone preconditioner and as a sub-preconditioner. AMG and SOR stagnate as a standalone preconditioner, while converge well as a sub-preconditioner under VCP. For all the cases, we used the first-order dual mortar approach on the coarse mesh. In terms of the VCP setting, we enabled adaptive variable condensation and assumed diagonal coupling between the Lagrange multiplier and the displacement variables. Figure 7 shows the performance of VCP with different sub-preconditioner types in terms of total wall time and total number of linear iterations. VCP can pretty efficiently converge using AMG and SOR, whereas the standard preconditioner stagnates or diverges. For the other sub-preconditioner types, VCP is still more efficient than the standard preconditioner, despite the additional computational cost from the variable condensation step (see Section 3). This is because a better-conditioned system is obtained after static condensation of the Lagrange multipliers

(see Figure 8). Meanwhile, the recent effort in memory preallocation and DoF indexing improvements described in Section 3.2 greatly reduce the overhead from the additional variable condensation steps.

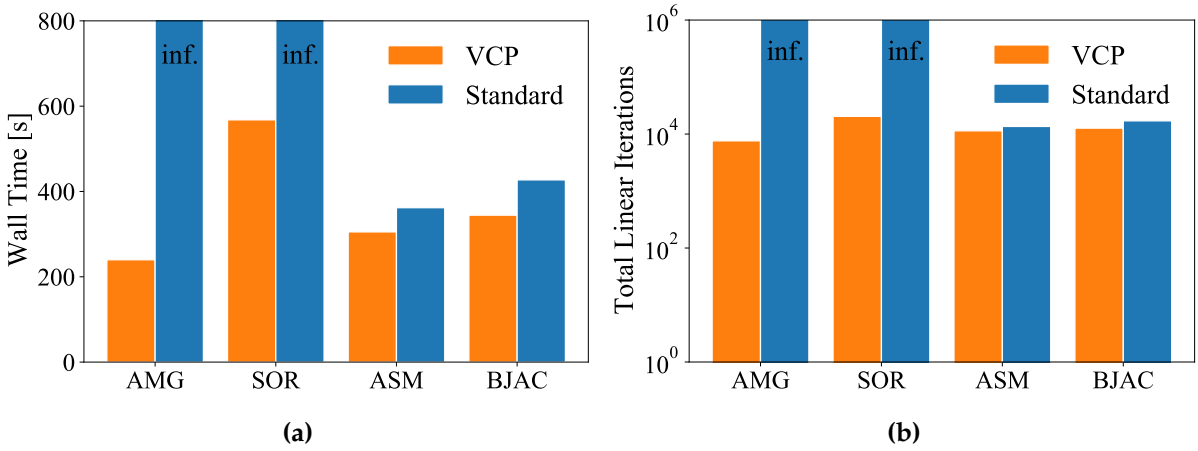

Figure 7: Performance of VCP for the Hertzian problem. Different sub-preconditioner types are utilized for comparison. Results are shown for four processors. Note the "inf." identifies the case when the solver stagnates thus the wall time and total number of iterations go to infinity.

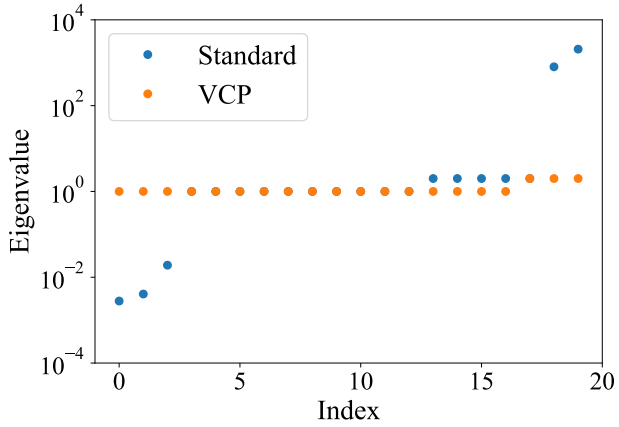

Figure 8: The smallest 20 eigenvalues of the Jacobian matrix using VCP and using standard approaches. While using VCP, the smallest eigenvalues are removed thus a better-conditioned system is obtained. Note the largest eigenvalues since are identical for the VCP and the standard approach thus is not shown here.

4.2 Ironing problem

As a second benchmark problem, we present a semi-circular tool intruding into a rectangular block, as illustrated in Figure 9. The tool is first pressed into the block to a prescribed displacement of $u_y = 1.2$ from 0.0 s to 2.0 s, then slides along the block from 2.0 s to 8.0 s until a horizontal displacement of $u_x = 8.0$ is reached. This typical problem is often referred to as an "ironing problem" in mechanical contact studies (see [3, 7]). For simplicity, we assume finite strain elastic stress behavior in both the tool and the block. We utilize $E = 6896.0$, $\nu = 0.32$ for the tool, and $E = 689.6$, $\nu = 0.32$ for the block. Some characteristic stages of deformation are shown in Figure 10. For comparison, we ran the same problem using both the node-on-face and mortar (standard and dual) formulations. In all cases, we employed first-order interpolation. Note that here, the node-on-face contact requires large normal vector smoothing parameters (which modify the mesh contact geometry) to run to completion. Mortar contact runs to completion without needing this mesh geometry artifact.

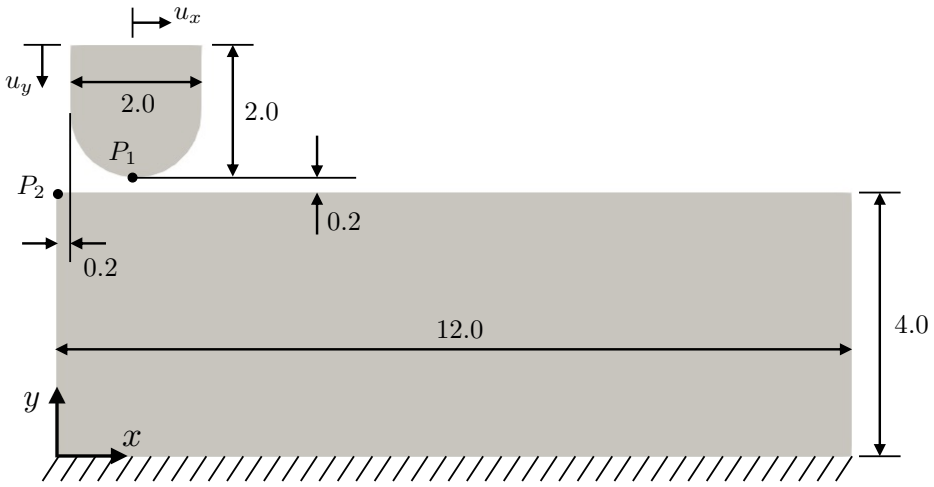

Figure 9: Ironing example of tool and block. Dirichlet boundary conditions are applied to the top surface of the tool.

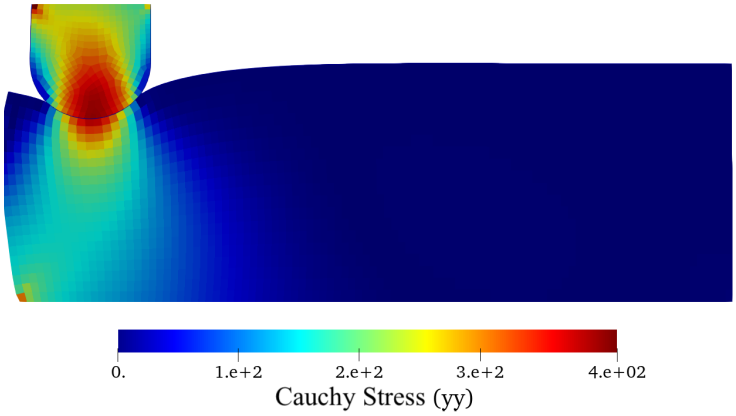

(a) $t = 2$s

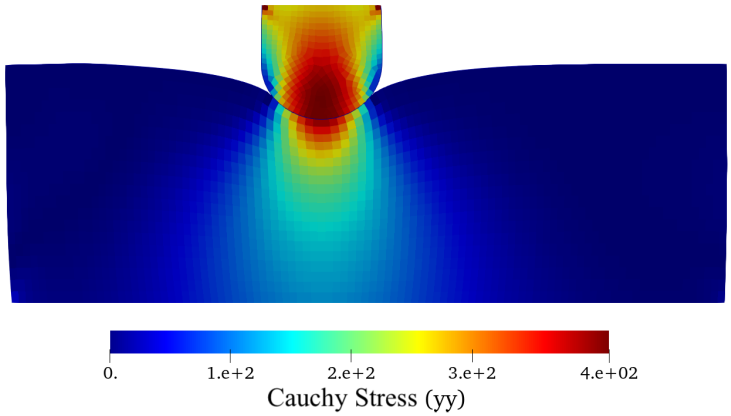

(b) $t = 5$s

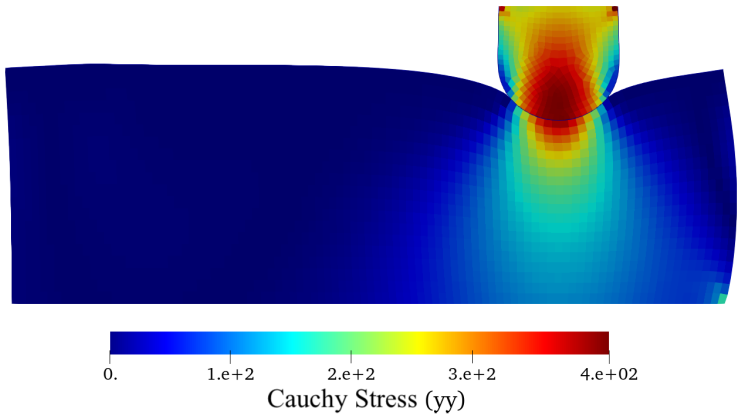

(c) $t = 8$s

Figure 10: Stress fields at three different time steps. The absolute value of the y directional Cauchy stress (σ_{yy}) is shown in all cases.

Figure 11 shows the contact pressure along the contact interface for a symmetric deformation state at $t = 5$ s. The results are shown for both contact formulations. It can be seen that both node-on-face and standard mortar introduce certain degrees of oscillations to the contact

pressure profile. Dual mortar produces a very smooth representation of the contact pressure profile, even though the results are based on a very coarse mesh with only 12 elements along the secondary interface.

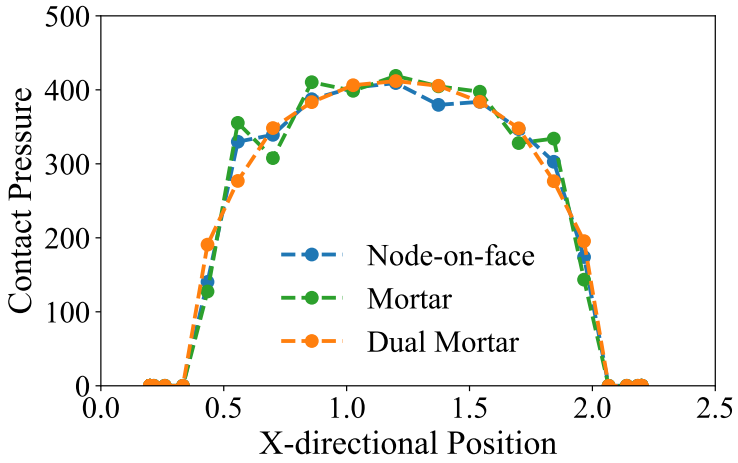

Figure 11: Contact pressure along the contact interface at $t = 5$ seconds (see Figure 10b). Results are shown for the mortar (standard and dual) and node-on-face formulations.

Figure 12 shows the nodal contact pressure history at the tip of the tool (i.e., P_1 in Figure 9). For comparison, the results are shown for both contact formulations. It can be seen that during the vertical motion of the tool, both the dual mortar and node-on-face approaches produce pretty smooth results, while standard mortar shows some oscillations. When the tool moves horizontally, node-on-face becomes highly oscillatory. This is a typical effect of the node-on-face approach when the contact nodes begin moving from one element to the next. Standard mortar is oscillatory too, due to numerical instabilities in the formulation. Dual mortar, on the other hand, removes the numerical artifacts.

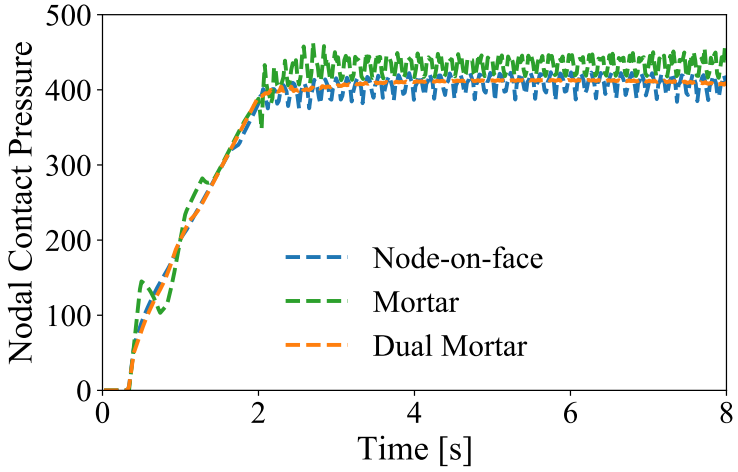

Figure 12: Contact pressure at the tip of the tool (i.e., point P_1 in Figure 9) with respect to time. Results are shown for the mortar (standard and dual) and node-on-face formulations.

Figure 13 shows the displacement history at the upper-left point of the substrate (i.e., P_2 in Figure 9). Both the x- and y-directional displacements are shown for both contact formulations. It can be seen that the node-on-face approach produces large oscillations for the x-direction displacement, due to the sliding of nodes between element faces. Standard and dual mortar produce relatively smooth displacement profiles in both directions.

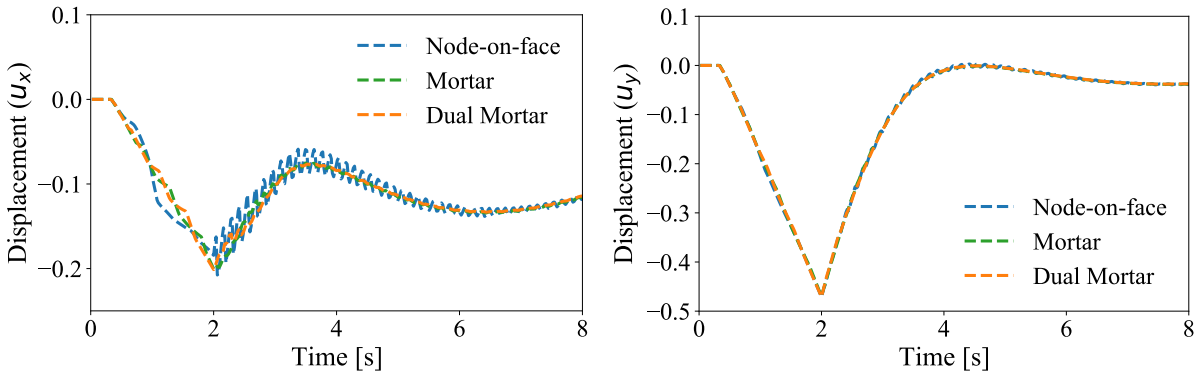

Figure 13: Displacement history at the tip of the substrate (i.e., point P_2 in Figure 9). (a) x-directional displacement. (b) y-directional displacement. Results are shown for mortar (standard and dual) and node-on-face formulations.

5 Thermomechanical contact with mortar in BISON

A number of typical BISON assessment cases were run using the traditional node-on-segment and recent mortar contact developments employing dual basis functions for the Lagrange multiplier interpolation. Note that in this section, we refer to the dual mortar approach as "mortar" and omit those standard mortar results shown to be oscillatory (see Section 4).

5.1 Pellet with missing surface

Two-dimensional plane-strain representations of fuel rods are commonly used in modeling nuclear reactors. These cross sections can potentially suffer from manufacturing defects, as described in [11], in which a discrete pellet with a missing pellet surface (MPS) defect is numerically modeled and analyzed in three dimensions. These defects may be included in the finite element analysis by modifying the circular cross section of the fuel pellet. Here, we simulate a flawed elastic fuel rod undergoing thermal expansion, creep, fission gas release, heat conduction, and coolant pressure. Power is increased linearly during the simulation. The fuel rod has a diameter of 8.62 mm, the initial gap between fuel and clad is 0.08 mm, the defect is 2 mm wide, and the cladding thickness is 0.61 mm. The initial geometry of the problem, along with the mortar contact pressure results, is depicted in Figure 14.

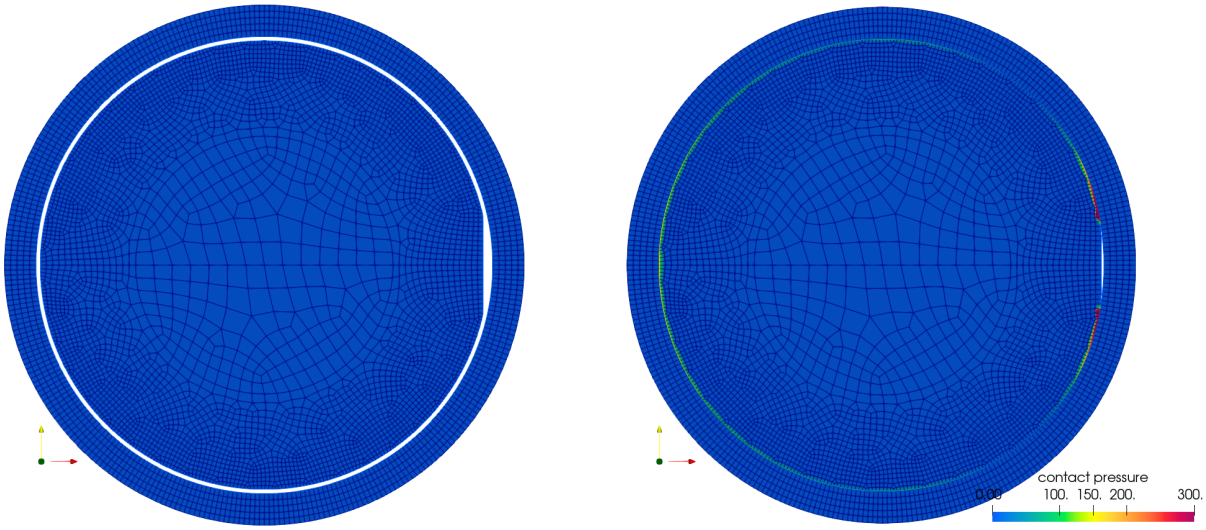

(a) Fuel rod cross section with an MPS defect (initial configuration)

(b) Contact pressure in the final stage of the simulation (mortar)

Figure 14: Circular fuel pellet cross section with an MPS defect.

As the cladding diameter decreases due to creep under high coolant pressure, the cladding constrains the radial expansion of the fuel. Two stages of this process are depicted in Figures 15 to 17, with Stage 2 representing a higher level of coolant pressure. The node-to-segment and mortar results show good agreement. In fact, the resulting temperature evolution difference on the fuel-cladding interface is negligible, as shown in Figure 15. However, artificial oscillations in the numerical contact pressure results—influenced by mesh discretization—are alleviated when enforcing the mechanical contact constraints in an integrated manner (see Equation (17)). Contact pressure results for pellet-clad mechanical interaction (PCMI) are shown in Figure 16. In Figure 17, improved results can be observed away from the defect's location, thanks to discretization-induced oscillations being significantly alleviated.

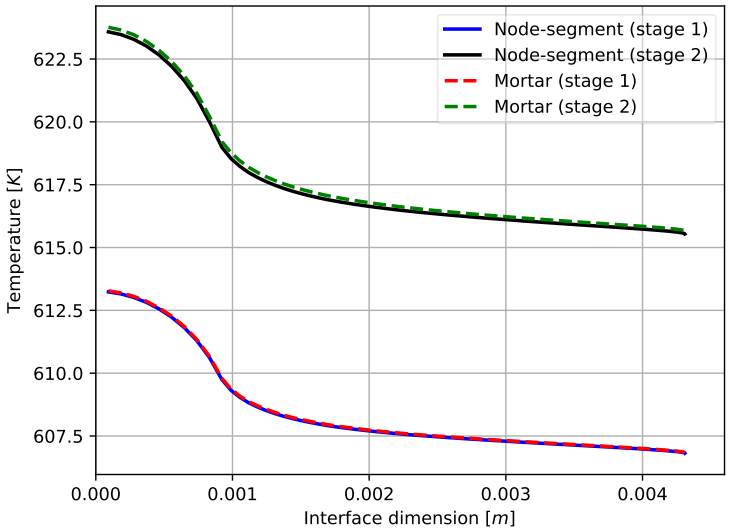

Figure 15: Temperature profile along the fuel surface for the quadrant of the model containing an MPS defect. The defect is located from 0 to 0.001 m.

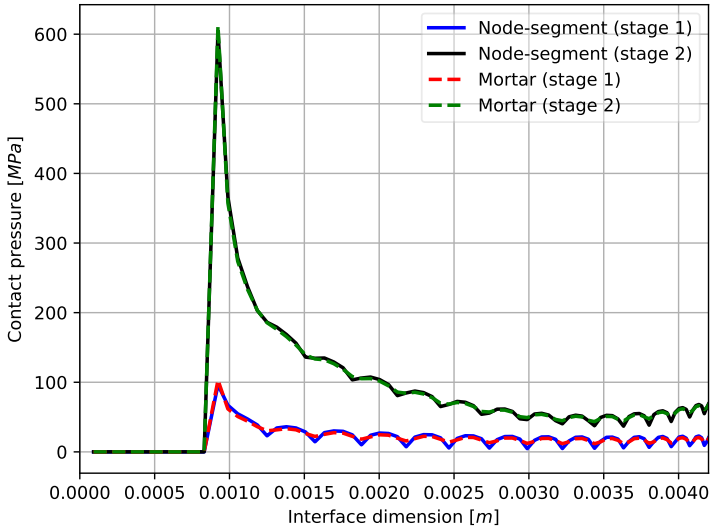

Figure 16: Contact pressure profile along the contact interface for the quadrant of the MPS defect model. The defect is located from 0 to 0.001 m.

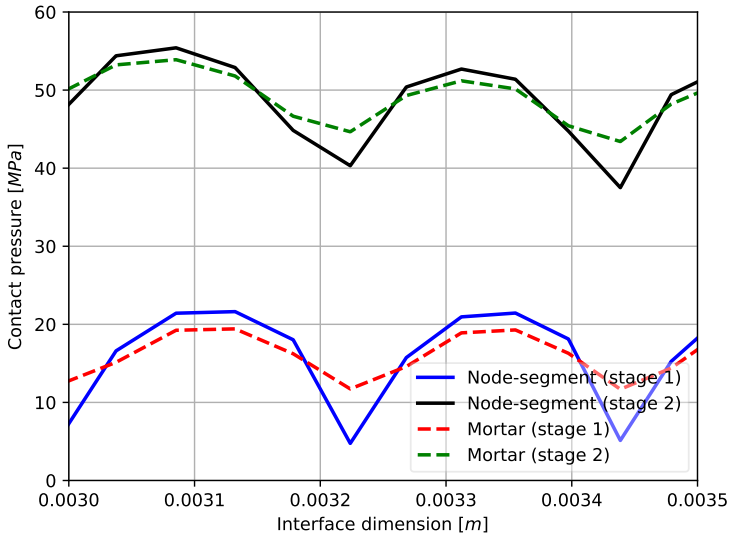

Figure 17: Zoomed-in view of the contact pressure profile of the MPS model in Fig. 16.

5.2 LWR fuel rods

In this section, we present the results of representative LWR fuel rod simulations using these contact methods. The thermomechanical contact and general gap heat transfer physics include thermal conductivities, specific heat, and elastic behavior. In addition, burnup, plenum pressure, and nuclear-specific material models are employed here. The problem is run using axisymmetric geometry assumptions and finite strain kinematics.

5.2.1 Smeared pellets

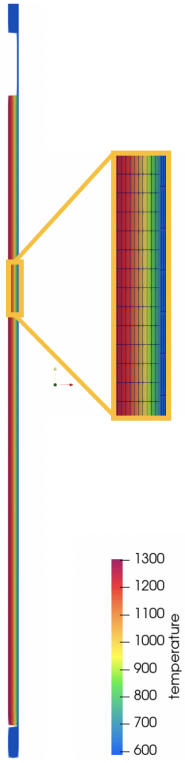

Figure 18: Depiction of the geometry and temperature results of the PK62 LWR fuel rod.

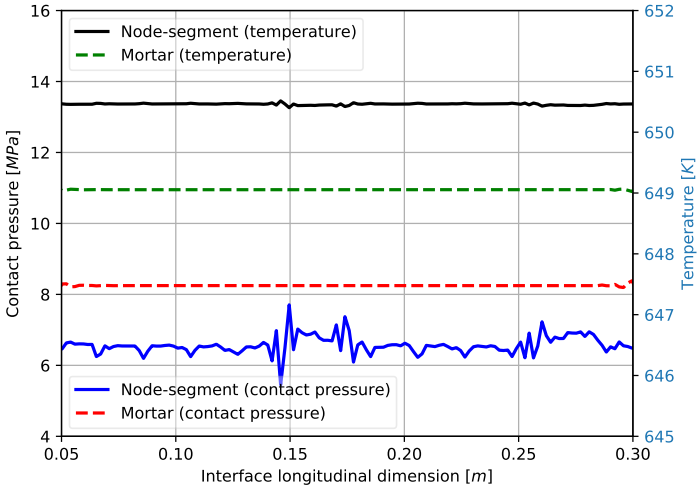

Figure 19: Spatial variation of temperature and contact pressure along a smeared LWR fuel rod at a stage of analysis in which the power is ramping up. While the temperature results are in close agreement, use of mortar enforcement increases the quality of the mechanical contact pressure results.

In this subsection, we present the numerical results of a pressurized water reactor with UO_2 pellets and Zircaloy-4 cladding. The test conditions and parameters are taken from test "PK62" of the Super-Ramp test series [2], in which high ramp rates were analyzed. This scenario features large grains, burnup within the range of 34–37 MWd/kgU, and linear heat ranges within 20–27 kW/m. For computational efficiency, 2-D axisymmetric models of LWR fuel rods commonly represent the fuel in a smeared fashion, with the entire fuel stack modeled as a single continuous body. This smeared representation of the pellets gives rise to a continuous interface between the outer fuel surface and the cladding (see Figure 18). Here, a typical smeared pellet model of a full fuel rod is run. A snapshot of interfacial thermomechanical variables is shown in Figure 19. When computed through mortar constraints, the thermal problem compares well against the traditional node-on-segment approach, with this latter approach showing minimal oscillations at locations far from the boundary. However, kinematic enforcement of contact constraints using a node-wise enforcement yields unphysical oscillations of significant amplitude, even on rod sections where boundary effects should be absent. Accurate prediction of contact pressure is important for these problems, as it affects gap thermal conductance and determines the accuracy of the mechanical solution. Oscillations in contact pressure could potentially result in higher stresses and increased material creep at high temperatures, possibly affecting predictions of rupture time and other quantities of engineering interest.

5.2.2 Discrete pellets

Using smeared pellet models is a simplification that may affect key simulation metrics. To more accurately represent local behavior, LWR fuel can also be modeled as a series of discrete pellets, as shown in Figure 20. The discretization of pellets adds a new numerical phenomenon to the LWR simulation's thermomechanical behavior: as the pellets move axially relative to the cladding, discontinuities in the contacting surfaces generate sudden changes in the contact interactions.

Here, a 10-pellet segment of an LWR fuel rod is simulated using both contact approaches. For the thermal problem, we increase the number of Gauss points to alleviate the numerical artifacts related to this discontinuous phenomenon that occurs when using the node-on-segment approach, whereas the corresponding numerical integration rule is employed for the mortar thermomechanical formulation (i.e., the minimum Gauss-Legendre quadrature rule order is employed to integrate the weak equations outlined in Section 2.3) (see, for example, Equation (17)).

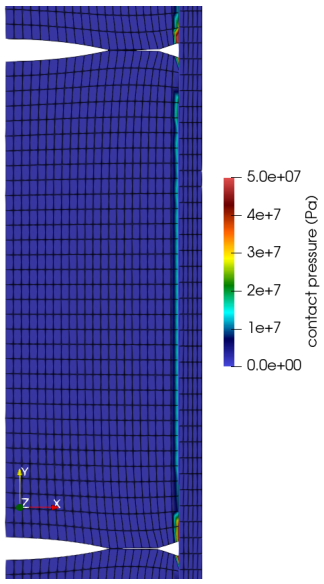

Figure 20: Detailed look at a discrete pellet's contact pressure in a 10-pellet LWR model.

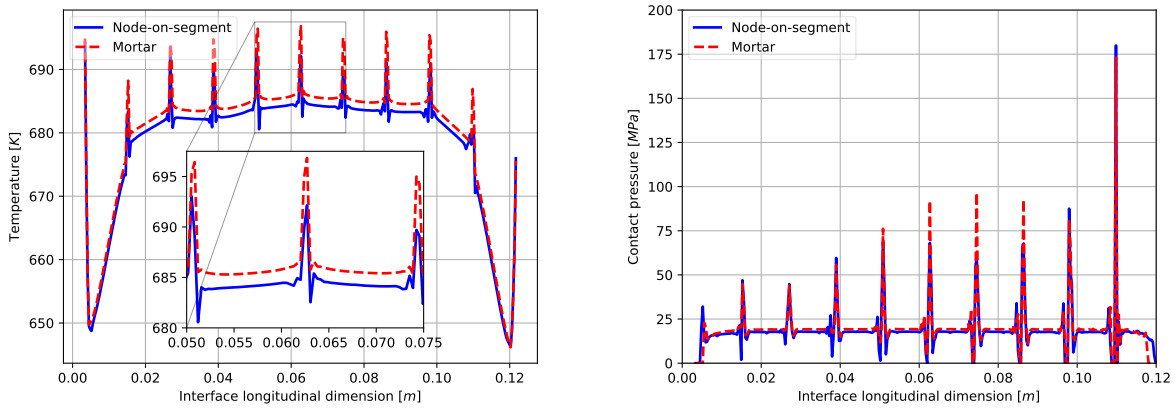

(a) Mortar/node-to-segment temperature distribution at the contact interface

(b) Mortar/node-to-segment contact pressure distribution at the contact interface

Figure 21: Comparison of results on the fuel-cladding interface for a discrete LWR fuel rod at full power.

Despite both mortar and node-on-segment approaches yielding almost identical results globally, a close look at Figure 21a reveals that mortar constraint enforcement reduces the temperature spatial oscillations at the pellet interface. Similarly, mortar contact pressure results feature fewer inflection points on discrete pellet interfaces (see Figure 21b). The time evolution of nodes near the center of the pellet (away from the rod's boundaries) is also of practical interest. Once mechanical contact is established, those material points are expected to undergo smooth contact pressure. The time evolution of such a node is shown in Figure 22. Despite this node being unaffected by model boundaries, the node-on-segment approach yields artificial oscillations, especially between 5.0 and $6.0 \cdot 10^7$ s (see Figure 22). This artificial, transient chatter cannot be removed by tightening solver tolerances, since it arises from

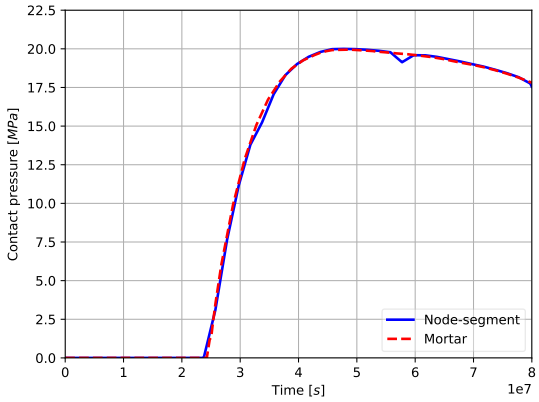

Figure 22: Time evolution of a discrete pellet's interface node contact pressure.

the node-on-segment formulation.

5.2.3 Discrete pellets with friction (mortar)

Use of friction in contact mechanic simulations is often problematic as it tends to hinder the solution convergence. The addition of friction increases the number of possible states of the nodes in contact, i.e. once in contact, each node can be in slipping or sticking states. These additional complexities can be tackled from different perspectives. A slip damper control can reduce the rate of change in the state of the nodes in contact; this can be achieved, for example, by limiting the reversal of the slip direction at nonlinear iterations, helping the system reach the state of equilibrium. Alternatively, BISON's simulations can use the augmented Lagrangian method (ALM), which solves the entire system iteratively, increasing the penalty factor used in the contact constraints until convergence is reached [13]. Use of ALM can effectively address frictional nonlinearities when using node-on-segment enforcement. However, there are challenging cases where frictional PCMI cannot be successfully solved with the NTS formulation, or where NTS requires too small time steps. This discrete-pellet case represents one such example in which the ALM with typical numerical parameters cannot reach convergence within reasonable turnaround.

Here, we use a definition of frictional mortar constraints based on Ref. [3] without additional algorithmic treatment. Frictional pressure results over the interface are shown in Figs. 23 and 24.

The tangential contact state of pellets with *high* and *low* frictional levels can be observed in Figs. 25a and 25b. Note that these results merely represent a numerical exercise. To accurately model the frictional behavior evolution on the pellet-cladding interface, more investigation is needed.

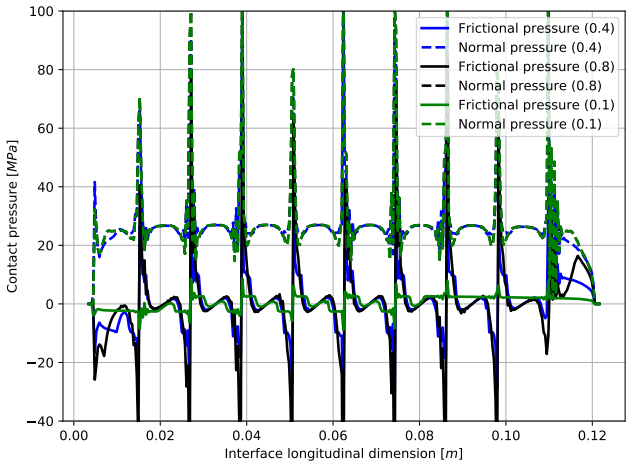

Figure 23: Frictional pressure results over the pellet-cladding interface at the final stage of the simulation for three values of the coefficient of friction: 0.8, 0.4, and 0.1. Note the spikes at the edges of the meshed discrete pellets.

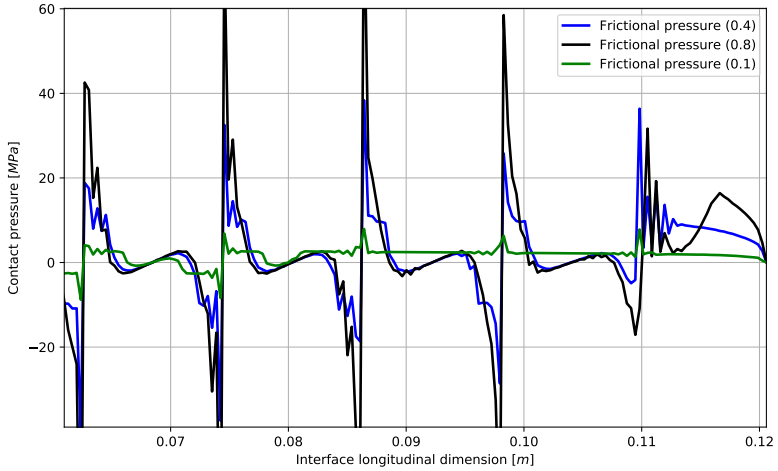

Figure 24: Frictional pressure detail over most elongated pellets. Changes in friction affect the longitudinal equilibrium of the system: Lower friction ($\mu = 0.1$, green line) causes the pellets to slide over the cladding surface.

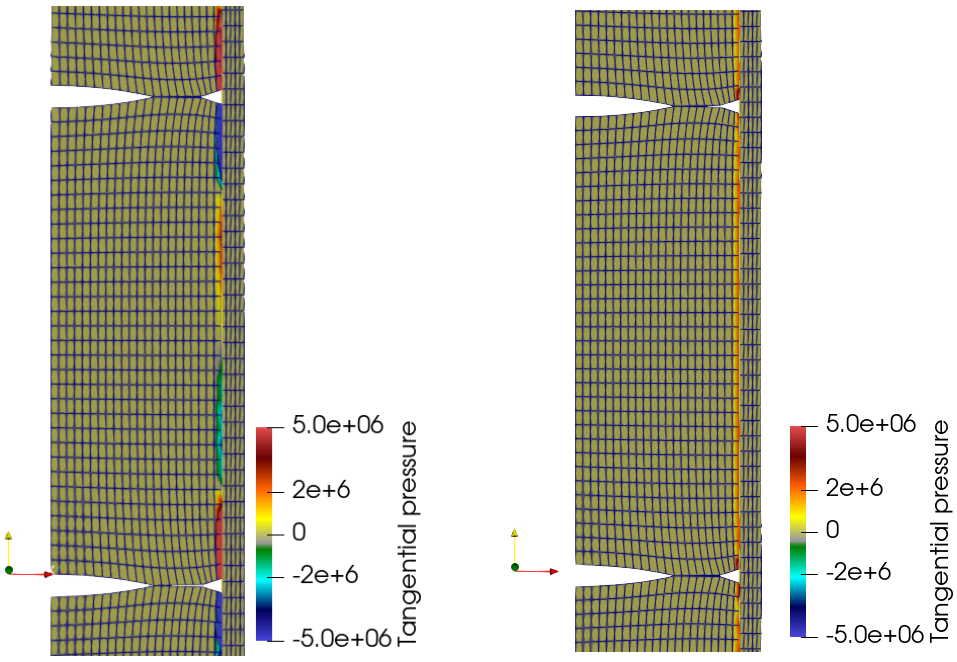

(a) Pellet in overall stick state ($\mu = 0.8$). **(b)** Pellet in overall slip state ($\mu = 0.1$).

Figure 25: Comparison of pellet's frictional states at the final stage of the simulation. Whereas relatively high values of friction cause a sticky pellet-cladding interface (see Fig. 25a), low values of friction change the overall system's equilibrium and allow pellet-cladding relative tangential displacement (see Fig. 25b).

5.3 Application of VCP in BISON

As described in Section 3, a new preconditioner type, i.e. VCP, is developed and tested with mortar-based mechanical and thermomechanical contact problems. During this FY, we took a step further by applying VCP to BISON assessment cases that couple thermomechanical contact with nuclear physics. Specifically, the smeared-pellet UFE019 case and the discrete pellet example of Section 5.2.2 (with frictionless contact) are tested. In this process, several issues are identified and efforts are made to fix them.

An initial profiling of the cases using VCP reveals that heavy computation (around 80% of total compute time) is spent on the condensation and creation of the reduced system of equations. Particularly, the initialization of the reduced system of equations was identified as a bottleneck. To address this issue, memory estimate and preallocation for the reduced system of equations are implemented, and the calculation of the condensed system is simplified. These changes help reduce the compute time spent on the condensation step from 80% to around 30% of the total compute time. Moreover, we improved the efficiency of DoFs indexing by using hash map instead of searching in vectors. This improvement further reduces the cost of the condensation step from 30% to less than 5%. With this recent improvement, performance of LU as a sub-solver under VCP is running at a similar speed as using LU as a stand-alone solver for the discrete pellet example (see Table 1), despite the overhead in the condensation step.

Solver Type	Linear Iteration Number	Nonlinear Iteration Number	Compute Time [sec]
VCP	3251	421	1120
LU	3394	422	1175

Table 1: Performance comparison of VCP using LU as a sub-solver with LU as a stand-alone solver. Results are shown for the discrete pellet example in BISON using eight processors.

In addition to profiling and reducing the compute time, we employed BoomerAMG as a subsolver under VCP. It is observed that BoomerAMG stagnates at the initial step of the simulation, which happens before the fuel comes into contact with the cladding. Removing contact from the simulation, however, did not improve the performance of BoomerAMG. Therefore, to successfully use VCP with iterative subsolvers in typical BISON cases, effort needs to be made towards successfully applying iterative solvers, such as BoomerAMG, on nuclear and mechanical physics –without contact.

5.4 Novel reactor geometry

We demonstrate the new thermo-mechanical mortar contact capability on a surrogate geometry similar to geometries that can be found in novel reactor concepts, a hexagonal arrangement of reflectors, moderators, fuel, and coolant channels in a monolithic structural block.

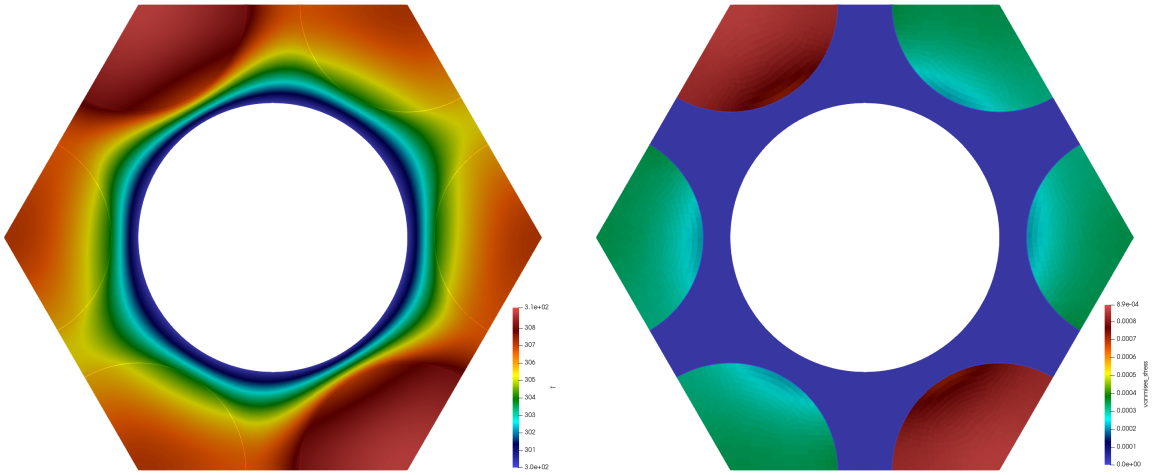

Figure 26: Temperature (left) and von Mises stress (right) distribution in the surrogate micro reactor model, computed using mortar based thermo-mechanical contact.

For the demonstration case we place a heat source in the two cylinder segments on the top left and bottom right (fuel blocks). We set different thermal expansion coefficients in all three distinct regions of the model, $10^{-4}\mathrm{K}^{-1}$ in the two fuel blocks, $10^{-7}\mathrm{K}^{-1}$ in the monolith, and $5 \cdot 10^{-5}\mathrm{K}^{-1}$ in the remaining four blocks. We set six contact surface pairs along the six 1/3 circle gaps between the monolith and the six cylinder segments in each corner. The resulting temperature and von Mises stress distributions are shown in Fig. 26.

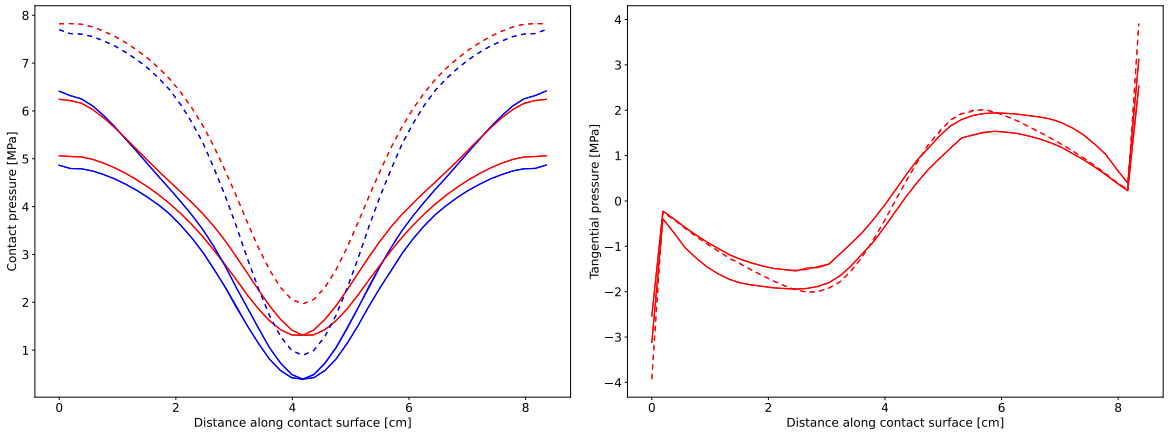

Figure 27: Normal (left) and tangential (right) contact forces along the six contact surfaces. Dashed lines indicate the two fuel surrogate blocks. Blue curves are obtained with frictionless mortar contact and red curves are obtained with frictional mortar contact. Note the spike in tangential contact at the ends of the contact surfaces. We have identified this issue with partially covered elements and are working on resolving it.

We show the normal and tangential contact pressures in Fig. 27. The contact pressures of the top left and bottom right cylinder segments are are plotted with dashes. The blue curves show the normal contact pressure with frictionless contact. Note that the tangential pressure at the ends of the contact surface is exhibiting nonphysical artifacts to to the missing edge contact implementation. This item remains as future work for FY22.

5.5 Migration guide

Thermomechanical mortar contact constraints have been successfully applied to typical BISON cases such as two-dimensional, axisymmetric, smeared-pellet, and discrete-pellet models. Result quality is often improved and initial application to frictional fuel-cladding mechanical interaction shows it has the potential to take much larger time steps than the ALM when used with the NTS formulation. For these reasons, next suggested steps involve wider adoption of the thermomechanical mortar framework in typical nuclear fuel analysis. To facilitate that process, a migration guide was created in BISON (see Fig. 28).

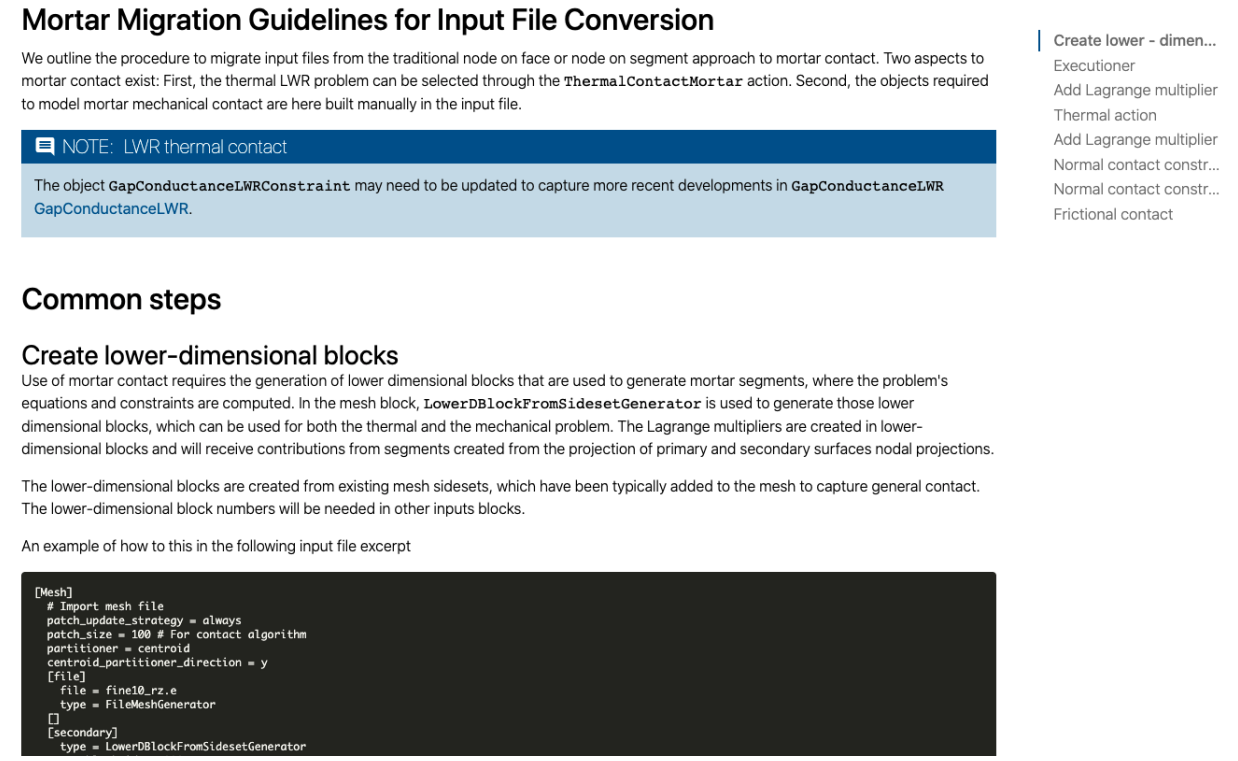

Figure 28: Snapshot of the mortar migration guide in BISON documentation. The guide describes the necessary steps to convert LWR's traditional input files to use MOOSE/BISON's thermomechanical contact framework.

Broader use of thermomechanical mortar will allow to perform improvements to the implementation and increase its robustness.

6 Conclusions and future work

The work carried out during FY21 has led to the following accomplishments:

- Consistent creation of mortar segments by choosing the secondary surface's nodal normal vectors to project primary and secondary surface nodes. Contact constraints now use normal vectors from the mortar segment field. Updates to mortar segment generation enable more complex simulation scenarios in which oblique projections are handled.
- Implementation of variationally consistent normal and frictional mechanical contact constraints, based on weighted quantities.
- Implementation of VCP to enable usage of iterative preconditioners and solvers for mortar-based mechanical and thermomechanical problems.
- Application of thermomechanical mortar to representative BISON assessment cases, including smeared-pellet, discrete-pellet, two-dimensional, and axisymmetric pellet cladding contact interaction models.
- Verification of mortar approaches on benchmark problems.

- Improvements on the performance and robustness of VCP.
- Initial investigation of applying VCP on BISON assessment cases.

It is important to emphasize that the demonstrated ability to use VCP with iterative preconditioners represents a significant step toward having the ability to use scalable iterative solvers on large problems. As has been demonstrated in this report, iterative solvers perform poorly on contact problems when VCP is not used. Because of this, BISON simulations have typically employed parallel direct solvers, which are limited in their ability to solve very large models.

In addition, the improved smoothness of the dual mortar algorithm demonstrates that this is a viable technique that has the potential to address longstanding deficiencies with frictional contact enforcement in BISON.

To generalize the existing contact capabilities and enable their efficient use for emerging reactor designs, longer-term tasks still remain. One key aspect is the extension of mortar constraints to simulate 3-D problems. The most significant development effort in this respect is the creation of general 2-D segments (or element projections). These segments can also be employed in a Nitsche formulation for mechanical contact. In addition, to capture multibody contact, as required for new reactor designs, it will also be necessary to generalize contact implementations to allow for interactions among more than two bodies. Finally, to efficiently run large systems with contact, more work is required to optimize the use of iterative solvers and better parallelize contact searches.

References

[1] Cichosz, T. and Bischoff, M. (2011). Consistent treatment of boundaries with mortar contact formulations using dual lagrange multipliers. *Computer Methods in Applied Mechanics and Engineering*, 200(9-12):1317–1332.

[2] Djurle, S. (1984). Final Report of the Super–Ramp Project. Technical Report STSR–32, Studsvik Energiteknik, AB.

[3] Gitterle, M. et al. (2010). Finite deformation frictional mortar contact using a semi-smooth newton method with consistent linearization. *International Journal for Numerical Methods in Engineering*, 84(5):543–571.

[4] Papadopoulos, P. and Taylor, R. L. (1992). A mixed formulation for the finite element solution of contact problems. *Computer Methods in Applied Mechanics and Engineering*, 94(3):373–389.

[5] Peterson, J. W. (2018). Progress toward a new implementation of the mortar finite element method in moose.

[6] Popp, A. (2012). *Mortar Methods for Computational Contact Mechanics and General Interface Problems*. PhD thesis, Technische Universität München.

[7] Popp, A., Gee, M. W., and Wall, W. A. (2009). A finite deformation mortar contact formulation using a primal–dual active set strategy. *International Journal for Numerical Methods in Engineering*, 79(11):1354–1391.

[8] Popp, A. and Wall, W. (2014). Dual mortar methods for computational contact mechanics–overview and recent developments. *GAMM-Mitteilungen*, 37(1):66–84.

[9] Schwen, D. et al. (2020). Summary of BISON documentation and UX milestones - NEAMS FY20 report.

[10] Seitz, A. et al. (2016). Isogeometric dual mortar methods for computational contact mechanics. *Computer Methods in Applied Mechanics and Engineering*, 301:259–280.

[11] Spencer, B. W. et al. (2016). 3D modeling of missing pellet surface defects in BWR fuel. *Nuclear Engineering and Design*, 307:155 – 171.

[12] Spencer, B. W. et al. (2018). BISON improvements for robustness and speed. Technical report, Idaho National Laboratory.

[13] Spencer, B. W., Peterson, J. W., Jiang, W., Lui, Y., Veeraraghavan, S., and Casagranda, A. (2017). Bison contact algorithm improvements in support of pellet cladding mechanical interaction modeling. 1(1).

[14] Wohlmuth, B. (2011). Variationally consistent discretization schemes and numerical algorithms for contact problems. *Acta Numerica*, 20:569–734.

[15] Yang, B., Laursen, T. A., and Meng, X. (2005). Two dimensional mortar contact methods for large deformation frictional sliding. *International journal for numerical methods in engineering*, 62(9):1183–1225.